



Retrieving the C and O Abundances of HR 7672 AB: A Solar-type Primary Star with a Benchmark Brown Dwarf

Ji Wang (王吉)¹ , Jared R. Kolecki¹ , Jean-Baptiste Ruffio² , Jason J. Wang (王劲飞)^{2,14} , Dimitri Mawet^{2,3} , Ashley Baker² , Randall Bartos³, Geoffrey A. Blake⁴ , Charlotte Z. Bond⁵, Benjamin Calvin^{2,6}, Sylvain Cetre⁷, Jacques-Robert Delorme^{2,7} , Greg Doppmann⁷, Daniel Echeverri², Luke Finnerty⁶ , Michael P. Fitzgerald⁶ , Nemanja Jovanovic² , Michael C. Liu⁸, Ronald Lopez⁶, Evan Morris⁹, Anusha Pai Asnodkar¹ , Jacklyn Pezzato², Sam Ragland⁷, Arpita Roy^{10,11} , Garreth Ruane^{2,3} , Ben Sappéy¹², Tobias Schofield², Andrew Skemer⁹ , Taylor Venenciano¹³, J. Kent Wallace³, Nicole L. Wallack⁴ , Peter Wizinowich⁷ , and Jerry W. Xuan²

¹ Department of Astronomy, The Ohio State University, 100 W 18th Avenue, Columbus, OH 43210, USA; wang.12220@osu.edu

² Department of Astronomy, California Institute of Technology, Pasadena, CA 91125, USA

³ Jet Propulsion Laboratory, California Institute of Technology, 4800 Oak Grove Drive, Pasadena, CA 91109, USA

⁴ Division of Geological & Planetary Sciences, California Institute of Technology, Pasadena, CA 91125, USA

⁵ UK Astronomy Technology Centre, Royal Observatory, Edinburgh EH9 3HJ, UK

⁶ Department of Physics & Astronomy, 430 Portola Plaza, University of California, Los Angeles, CA 90095, USA

⁷ W.M. Keck Observatory, 65-1120 Mamalahoa Hwy, Kamuela, HI, USA

⁸ Institute for Astronomy, University of Hawai'i, 2680 Woodlawn Drive, Honolulu, HI 96822, USA

⁹ Department of Astronomy & Astrophysics, University of California, Santa Cruz, CA 95064, USA

¹⁰ Space Telescope Science Institute, 3700 San Martin Drive, Baltimore, MD 21218, USA

¹¹ Department of Physics and Astronomy, Johns Hopkins University, 3400 N Charles Street, Baltimore, MD 21218, USA

¹² Center for Astrophysics and Space Sciences, University of California, San Diego, La Jolla, CA 92093, USA

¹³ Physics and Astronomy Department, Pomona College, 333 N. College Way, Claremont, CA 91711, USA

Received 2021 December 30; revised 2022 February 17; accepted 2022 February 18; published 2022 March 25

Abstract

A benchmark brown dwarf (BD) is a BD whose properties (e.g., mass and chemical composition) are precisely and independently measured. Benchmark BDs are valuable in testing theoretical evolutionary tracks, spectral synthesis, and atmospheric retrievals for substellar objects. Here, we report results of atmospheric retrieval on a synthetic spectrum and a benchmark BD, HR 7672 B, with `petitRADTRANS`. First, we test the retrieval framework on a synthetic PHOENIX BT-Settl spectrum with a solar composition. We show that the retrieved C and O abundances are consistent with solar values, but the retrieved C/O is overestimated by 0.13–0.18, which is about four times higher than the formal error bar. Second, we perform retrieval on HR 7672 B using high spectral-resolution data ($R = 35,000$) from the Keck Planet Imager and Characterizer and near-infrared photometry. We retrieve $[C/H]$, $[O/H]$, and C/O to be -0.24 ± 0.05 , -0.19 ± 0.04 , and 0.52 ± 0.02 . These values are consistent with those of HR 7672 A within 1.5σ . As such, HR 7672 B is among only a few benchmark BDs (along with Gl 570 D and HD 3651 B) that have been demonstrated to have consistent elemental abundances with their primary stars. Our work provides a practical procedure of testing and performing atmospheric retrieval, and sheds light on potential systematics of future retrievals using high- and low-resolution data.

Unified Astronomy Thesaurus concepts: [Exoplanet atmospheric composition \(2021\)](#); [Brown dwarfs \(185\)](#); [Chemical abundances \(224\)](#)

1. Introduction

Physical and chemical properties of substellar objects can be inferred by modeling observed spectra. When the spectral modeling contains the key physics and chemistry in a self-consistent way, we call it a forward-modeling approach. When the spectral modeling uses a flexible parameterization without a rigorous and self-consistent treatment of the involved physics and chemistry, we call it a free-retrieval approach. Both approaches are valuable in the study of atmospheres of exoplanets.

The majority of forward modeling and free-retrieval analyses have been applied to transiting planets (e.g., Waldmann et al. 2015; Zhang et al. 2021), see also a recent review by

Madhusudhan (2019). Fewer such analyses exist for directly imaged exoplanets (e.g., Konopacky et al. 2013), mainly because of the smaller number of targets. However, direct imaging of exoplanets is considered a top science goal for future extremely large telescopes (ELTs; e.g., Mawet et al. 2019) and NASA missions such as HabEx and LUVOIR (Gaudi et al. 2021). Toward the goals of (1) better understanding exoplanets' atmospheres and (2) ultimately detecting biosignatures via spectroscopic observations, we need to address the following challenges facing direct imaging of exoplanets.

First, while most spectral modeling frameworks (e.g., Baudino et al. 2017; Lavie et al. 2017; Mollière et al. 2019) are benchmarked against each other, they have not been tested against benchmark brown dwarfs (BDs), for which we know the dynamical mass (e.g., from radial velocity and/or astrometric measurements) and the chemical composition (e.g., from their companion primary stars). The chemical homogeneity assumption, that stars and BDs form within the same molecular cloud should have identical chemical compositions, has been tested and

¹⁴ 51 Pegasi b Fellow.

applied for solar-type and M-type companions (e.g., Mann et al. 2013; Nelson et al. 2021). Such benchmarking efforts have only been done using low spectral-resolution data for very limited number of BDs (GJ 570 D and HD 3651 B, Line et al. 2015).

Second, future data from ELTs are likely to include those with very high spectral resolution ($R \sim 100,000$), e.g., MODHIS at TMT (Mawet et al. 2019) and METIS at E-ELT (Brandl et al. 2021), but few existing spectral modeling frameworks can handle such high-resolution data. This drawback has been realized and recent advances have been made for transiting planets (e.g., Fisher et al. 2020).

Third, combining high- and low-resolution data presents a challenge. While theoretical frameworks have been proposed (e.g., Brogi et al. 2017) and applied to transiting planets (Gandhi et al. 2019), no such spectral modeling framework has been tested using benchmark BDs to better characterize directly imaged exoplanets.

The above challenges motivate the retrieval framework in this paper, which can be viewed as an extension of `petitRADTRANS` (Mollière et al. 2019). In this paper, we (1) test the framework against a synthetic PHOENIX spectrum with known solar composition and (2) apply the framework on a benchmark BD, HR 7672 B, whose stellar abundance is inferred from its G-type primary star HR 7672 A. We first provide an overview of recent progress in the spectral modeling of BDs and the nature of the HR 7672 AB system.

1.1. Recent Progress in Modeling BDs

Line et al. (2015) presented groundbreaking work where they showed that two benchmark T-type BDs (GJ 570 D and HD 3651 B) have similar C, O, and Fe abundances as their primary stars. T-type BDs were chosen because their cloudless atmospheres are simpler than cloudy atmospheres and require fewer modeling parameters. However, Maire et al. (2020) found evidence of patchy or thin clouds for a T-type benchmark BD, HD 19467 B. By comparing to a theoretical model grid and a BD spectral library, Rickman et al. (2020) studied another benchmark BD (HD 13724 B) but provided no C or O abundance. Zhang et al. (2021) used a forward-modeling approach to study three late-T-type benchmark dwarfs, HD 3651 B, GJ 570 D, and Ross 458 C and found discrepancies in temperature, radius, and surface gravity, which they attributed to clouds, reduced vertical temperature gradients, or disequilibrium processes. Kitzmann et al. (2020) used `Helios-r2` to retrieve the atmospheric properties of GJ 570 D and stressed the impact of chemical equilibrium on inferred C and O abundances.

There are more challenges in the L-type BD regime because of clouds. Burningham et al. (2017) performed retrieval analyses on two BDs: 2MASS J05002100+0330501 and 2MASSW J2224438015852 and found evidence of cloudy conditions, but failed to address the anomalously high CO abundance, which was attributed to unrecognized shortcomings in their retrieval model. Gonzales et al. (2020) conducted a similar study on the L- and T-type BD binary J14162408+1348263AB and found a consistent C/O ratio between the binary pair. Peretti et al. (2019) studied another L-type benchmark BD, HD 4747B. However, their retrieved C and O abundances were off by 1.0 and 0.4 dex (x dex corresponds to a factor of 10^x) from the primary star, which is a $\sim 2\sigma$ discrepancy.

1.2. HR 7672 A and B

HR 7672 A is a solar-type G0 star (Brewer et al. 2016). Due to the radial velocity trend of HR 7672 A, Liu et al. (2002) detected HR 7672 B, which is an L-type BD companion at a separation of $0''.8$. The estimated effective temperature was 1510–1850 K. Apparent J -, H -, and K -band magnitudes were reported in Boccaletti et al. (2003) with values of ~ 14.4 , 14.04 ± 0.14 , and 13.04 ± 0.10 . Crepp et al. (2012) refined the dynamical mass of HR 7672 B to lie between 65.6 and 71.1 M_{Jupiter} using combined radial velocity and astrometric data sets. With improved Gaia astrometry and a longer RV baseline, Brandt et al. (2019) further constrained the mass of HR 7672 B to be $72.7 \pm 0.8 M_{\text{Jupiter}}$. The rich literature on HR 7672 AB and the recently obtained high-resolution spectrum for HR 7672 B make the system an ideal benchmark to test retrieval frameworks.

The paper is organized as follows. Section 2 summarizes the observational data. We conduct an independent abundance analysis for HR 7672 A and in report the results in Section 3. Section 4 describes our framework of ultra-cool atmosphere retrieval. In Section 5, we test the framework using a PHOENIX BT-Settl spectrum with solar composition. In Section 6, we apply the framework to HR 7672 B to check if the retrieved abundances are consistent with the measured abundances from HR 7672 A. Finally, we summarize the paper in Section 7.

2. Data

We used archival high-resolution spectra to determine the primary stellar abundances. For the BD atmospheric abundances, we obtained high-resolution ($R = 35,000$) data using NIRSPEC fed by the Keck Planet Imager and Characterizer (KPIC, Mawet et al. 2018; Jovanovic et al. 2019; Delorme et al. 2020). To supplement the spectroscopic data, we also gathered photometric data for HR 7672 B. The photometric data serve as low-resolution data ($R \sim 3\text{--}5$) in our joint high- ($R \sim 35,000$) and low-resolution retrieval, and our retrieval code can handle any spectral resolution R between a few and 1,000,000.

2.1. Spectroscopic Data for HR 7672 A

Keck/HIRES spectroscopic data with wavelength coverage ranging from 4350 to 8690 Å was retrieved from the Keck Observatory Archive (KOA). These observations were taken on 2018 July 5 between 13:24:13 and 13:25:24 UTC (PI: Yong).

Using the associated calibration files, this raw data was then reduced into a one-dimensional spectrum using the MAKEE pipeline.¹⁵ The MAKEE reduction process involves wavelength scaling using calibration images (ThAr arcs), flat-field correction for large-scale continuum fluctuations, and CCD bias subtraction. The resulting signal-to-noise ratio at 7770 Å (near the O I triplet) is approximately 300.

2.2. Spectroscopic Data for HR 7672 B

HR 7672 B was observed in the K band ($R \sim 35,000$) with Keck/NIRSPEC/KPIC on three occasions summarized in Table 1. An A0 standard star, zet Aql, was observed each epoch to calibrate the combined transmission of the atmosphere and the instrument. The data were acquired and reduced following the approach described in Delorme et al. (2021).

¹⁵ <https://sites.astro.caltech.edu/~tb/makee/>

Table 1
K-band Observations of HR 7672 A and B with KPIC

Object	Date	Exposure Time	Note
zet Aql	2020-06-08	3 × 10 s	standard
HR 7672 B	2020-06-08	11 × 10 minutes	
zet Aql	2020-06-09	3 × 10 s	standard
HR 7672 B	2020-06-09	10 × 10 minutes	
zet Aql	2020-09-28	4 × 4.4 s	standard
HR 7672 B	2020-09-28	7 × 10 minutes	

Images were first background subtracted and bad-pixel corrected. The fiber trace locations and widths were calibrated using the standard star. The spectra were then extracted using optimal extraction (Horne 1986). The wavelength solution was derived from observations of the M-giant HIP 81497 using a forward model of the tellurics generated with the Planetary Spectrum Generator (Villanueva et al. 2018) and a Phoenix model of the star ($\log(g/[1 \text{ cm s}^{-2}]) = 1$; $T_{\text{eff}} = 3600 \text{ K}$ Husser et al. 2013).

To obtain the normalized spectra, we perform the following procedures. First, we subtract background from both the target star and the telluric standard star. Second, we divide the target star spectrum by the telluric standard star spectrum to remove the blaze function and telluric lines. Third, we normalize the target star spectrum by dividing by the median of the spectrum. The median spectrum is obtained by running a median kernel with width of 200 pixels. The kernel width, which is about one tenth of the entire spectral order, is selected in order not to affect the molecular absorption lines/bands. Finally, we shift the normalized spectra by a certain radial velocity. The radial velocity is determined by cross-correlating the spectrum of each date with a PHOENIX synthetic spectrum (Allard et al. 2012, 2013; Baraffe et al. 2015, and references therein) with T_{eff} of 1600 K, $\log(g)$ of 5.5, and solar abundances.

KPIC data sets for HR 7672 B are shown in Figure 1. We use two (out of nine) spectral orders centering around 2.25 and 2.31 μm . For other orders, we cannot calibrate the wavelength, the signal-to-noise ratio is too low, these orders are heavily contaminated by telluric CO₂ lines.

2.3. Photometric Data for HR 7672 B

We used *J*-, *H*-, and *K*-band differential magnitudes (Crepp et al. 2012) to convert to apparent magnitudes. In the conversion, magnitudes from HR 7672 A are from SIMBAD. The apparent magnitudes are then converted to physical flux in the unit of $\text{W } \mu\text{m}^{-1} \text{ m}^{-2}$, assuming a distance of $17.72 \pm 0.02 \text{ pc}$ (Gaia DR2, Gaia Collaboration et al. 2016, 2018). As such, we adopt 1.5×10^{-15} , 1.8×10^{-15} , and $1.4 \times 10^{-15} \text{ W } \mu\text{m}^{-1} \text{ m}^{-2}$ for the *J*-, *H*-, and *K*-band, respectively. The fractional uncertainties for *J*-, *H*-, and *K*-band fluxes are measured to be 20%, 12%, and 9% (Crepp et al. 2012). Note that the *J*-band flux and the associated error are likely to be affected by speckle contamination (Boccaletti et al. 2003).

We measured the *L'*-band of HR 7672 B using Keck/NIRC2 imaging data from the KOA taken on 2002 October 27 (PI: Graham). We used a total of 40 frames with 0.018 s exposures and 500 coadds. The images were sky subtracted using sky images taken after the sequence. Because the images were taken in position angle mode, no differential imaging techniques could be used. Instead, we registered all of the frames together by fitting the star in each image with a 2D Gaussian model and combined all of

the images together. HR 7672 B fortunately lies between the diffraction spikes from the primary star, so is visible after simple mean combination of frames (Figure 2). To moderately improve the detection, we subtracted a copy of the image that was rotated by 180° to remove symmetric features in the stellar PSF. We then fit a 2D Gaussian model to the brown dwarf companion, and measured a flux ratio of $(1.3 \pm 0.3) \times 10^{-3}$ in *L'*-band. This leads to a *L*-band flux of $(5.5 \pm 1.3) \times 10^{-16} \text{ W } \mu\text{m}^{-1} \text{ m}^{-2}$.

3. Stellar Atmospheric Parameters and Abundances of HR 7672 A

We performed our stellar parameter derivation, abundance measurements, and error analysis using the same code and 1D-LTE analysis process explained in Sections 5.1 through 5.3 of Kolecki et al. (2021). We present a brief overview here. The results are reported in Tables 2 and 3.

3.1. Stellar Parameters

3.1.1. Effective Temperature and Surface Gravity

We derived T_{eff} and $\log(g)$ by comparing magnitudes from Gaia (*G*, *Bp*, *Rp*), 2MASS (*J*, *H*, *Ks*), and WISE (W1, W2, W3, W4) with theoretical stellar isochrones from the Dartmouth Stellar Evolution Database¹⁶ (Dotter et al. 2007).

At a fixed metallicity, we calculated the sum of the differences (i.e., residuals) between observed and isochronal values for each passband magnitude along an age-equivalent evolutionary phase isochrone grid. A contiguous area where the residuals are within 10% of their absolute minimum on the grid is chosen as valid points on this isochrone grid to extract T_{eff} and $\log(g)$ values from. We took the mean of all these resulting values as the final parameters.

3.1.2. Microturbulence (ξ)

To determine a value for the microturbulence velocity (ξ), we first fixed T_{eff} and $\log(g)$, then minimized the slope of the correlation between abundance and reduced equivalent width by calculating the slope for a grid of microturbulence velocities and interpolating to find the velocity where the slope was equal to 0.

Uncertainty in the microturbulence parameter was determined by perturbing the value until the slope fell outside the range of uncertainty defined by the linear regression fit.

3.2. Abundances

The use of *abfind* in MOOG (Snedden 1973) requires measurement of the equivalent widths of spectral absorption lines. This was done using a semi-automated program. This program displays measurements from fits of both a Gaussian profile and a Voigt profile to each line, along with its direct measurement of the observed data.

From these three options, we chose the method that most closely fit trends in the data. This manual screening process allows for the most accurate measurements to be kept for all lines, mitigating the effects of noise, contamination, and improper line fitting. If these effects were too great, we discarded the line from the final line list.

¹⁶ <http://stellar.dartmouth.edu/models/>

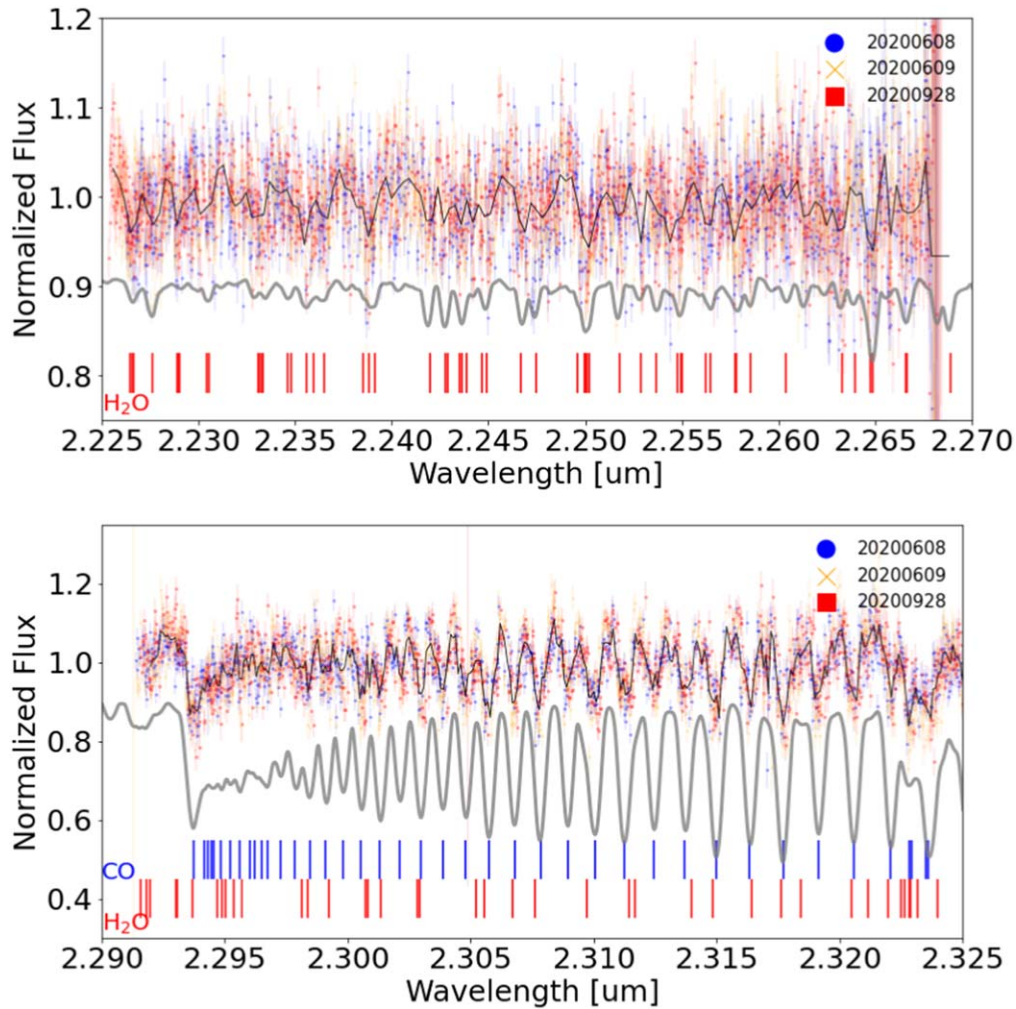


Figure 1. KIPAC data were obtained on UT 2020 June 8 (blue circles), 2020 June 9 (yellow crosses), and 2020 September 28 (red squares) and we use two spectral orders (top and bottom panels) for the analyses in this paper. Black lines through the data points are binned spectra with a bin size of 1 Å. For comparison, a PHOENIX BT-Settl spectrum with a T_{eff} of 1600 K, $\log(g)$ of 5.5, and $v \sin i$ of 40 km s^{-1} is shown in gray. Prominent CO and H_2O line locations are marked as blue and red vertical lines.

To mitigate the effects of strong line damping on our results, we chose a maximum equivalent width of 100 mÅ, and ignored all lines stronger than this cutoff.

Uncertainties in all abundances were calculated according to the method outlined in Epstein et al. (2010). This method takes the base uncertainty to be the standard deviation of the mean abundance, and modifies it to account for uncertainty and covariances in the atmospheric parameters.

Wavelength, excitation potential, and $\log(gf)$ data for Fe, C, and O lines was supplied by the NIST Atomic Spectra Database (Kramida et al. 2020). Solar abundances were taken from Palme et al. (2014).

3.2.1. Iron Abundances and $[\text{Fe}/\text{H}]$

Once the iteration of stellar parameters was completed, we determined initial $[\text{Fe I}/\text{H}]$ and $[\text{Fe II}/\text{H}]$ values of -0.07 ± 0.07 dex and -0.06 ± 0.08 dex respectively, relative to the adopted solar iron abundance of 7.48 (Palme et al. 2014).

From these values, we aimed to use correction tables to account for the limitations of a 1D-LTE (one-dimensional local thermodynamic equilibrium) analysis. Amarsi et al. (2019) have calculated a grid of 3D-LTE/1D-LTE corrections for several

Fe II lines which we have used to adjust our Fe II abundance measurement.

Using the point on the grid ($T_{\text{eff}} = 6000 \text{ K}$, $\log(g) = 4.5$, $\xi = 1.0 \text{ km s}^{-1}$, $[\text{Fe}/\text{H}] = 0.00$) that most closely matches the 1D-LTE parameters of HR 7672, we found that the average correction for the Fe II lines we measured results in an increase of this abundance by 0.05 dex. Thus, we report our final $[\text{Fe II}/\text{H}] = -0.01 \pm 0.08$.

Taking the overall metallicity ($[\text{Fe}/\text{H}]$) to be equal to the average of the Fe I and Fe II abundances and accounting for the effect this has on the uncertainty, $[\text{Fe}/\text{H}] = -0.04 \pm 0.07$.

3.2.2. LTE C and O Abundances

We then proceeded to derive the abundances of carbon and oxygen. The oxygen abundance was derived from the O I 777 nm triplet feature, while carbon abundance was derived from lines at 5380.32, 6587.62, 7113.17, 7115.17, and 7116.96 Å. From these line features, we found LTE abundances of $\log(\epsilon_{\text{C}}) = 8.42 \pm 0.05$ and $\log(\epsilon_{\text{O}}) = 8.88 \pm 0.06$, where ϵ_X is the abundance for element X and ϵ_{H} is defined at 10^{12} . The C and O abundances correspond to $[\text{C}/\text{H}]$ and $[\text{O}/\text{H}]$ of -0.08 ± 0.05 dex and 0.15 ± 0.06 dex, respectively.

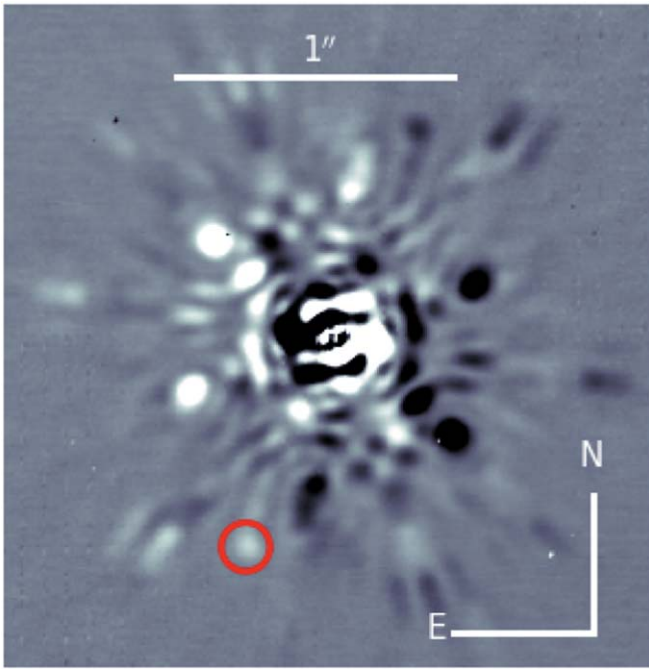


Figure 2. L' -band image of HR 7672 B (indicated by the red circle). The image is shown in linear scale with saturation at 10% of the maximum value.

3.2.3. Consideration of Non-LTE Effects on C and O Abundances

As the abundance derived from the O I triplet is known to be affected significantly by the LTE assumption, we used the grid of 3D non-LTE (NLTE) corrections calculated by Amarsi et al. (2019) to account for this.

Taking the point on this grid ($T_{\text{eff}} = 5999$ K, $\log(g) = 4.5$, $\xi = 1.0$ km s $^{-1}$, $[\text{Fe}/\text{H}] = 0.00$, $\log(\epsilon_{\text{C}}) = 8.43$, $\log(\epsilon_{\text{O}}) = 8.89$) that most closely matches the LTE parameters of HR 7672, we find that the NLTE corrections lower $[\text{O}/\text{H}]$ by 0.22 dex and $[\text{C}/\text{H}]$ by 0.01 dex. We note that, while the carbon NLTE correction is within the uncertainty of $[\text{C}/\text{H}]$, it does affect the final C/O ratio.

After the NLTE corrections were applied, our final C and O abundances were determined to be $\log(\epsilon_{\text{C}}) = 8.41 \pm 0.05$ and $\log(\epsilon_{\text{O}}) = 8.66 \pm 0.06$, corresponding to $[\text{C}/\text{H}]$ and $[\text{O}/\text{H}]$ of -0.09 ± 0.05 and -0.07 ± 0.06 dex.

This leads to an adopted $\text{C}/\text{O} = 0.56 \pm 0.11$, where the uncertainty of C/O is given by adding in quadrature the fractional uncertainty of the numerical quantities of C and O and multiplying the result by the C/O value.

3.3. Comparing to Previous Work

HR 7672 A was included in the abundance analysis samples of da Silva et al. (2015), Brewer et al. (2016), and Luck (2017), though the first did not include an $[\text{O}/\text{H}]$ measurement. Each derived an effective temperature within 30 K of the value adopted in this paper, within the 1σ uncertainty range. Each also derived a $\log(g)$ value within 0.03 dex of our photometric measurement.

Our $[\text{Fe}/\text{H}]$ measurement is consistently below but in agreement with those of the literature by $\sim 1\sigma$. A similar consistency level is found in the carbon and oxygen abundances. Our $\log(\epsilon_{\text{C}})$ is within 1σ of the values derived by Brewer et al. (2016) and Luck (2017),

Table 2

Stellar Parameters Derived by this Paper and by da Silva et al. (2015), Brewer et al. (2016), and Luck (2017)

	T_{eff}	$\log(g)$	ξ (km s $^{-1}$)	$[\text{Fe}/\text{H}]$
This work	5946 ± 40	4.43 ± 0.01	0.81 ± 0.16	-0.04 ± 0.07
da Silva et al. (2015)	5972 ± 34	4.44 ± 0.14	1.03 ± 0.08	0.08 ± 0.05
Brewer et al. (2016)	5940 ± 25	4.40 ± 0.03	...	0.07 ± 0.01
Luck (2017)	5946	4.40	1.21	0.04 ± 0.16

and within 2σ of the value derived by da Silva et al. (2015). Our $\log(\epsilon_{\text{O}})$ is consistent to within 1σ with both mentioned papers that also measured the abundance of oxygen. For more information, values from each paper are compared with our results in Tables 2 and 3.

We note that Luck (2017) does not provide values for uncertainties of C and O, but does provide error bars in plots of these chemical abundances (Figure 13 of that paper). We compared the length of these bars with the scale of the axes in order to get numerical values for use in Tables 2 and 3.

4. Atmosphere Modeling and Retrieval for HR 7672 B

4.1. Overview of the Modeling and Retrieval Framework

Our framework to model exoplanet atmospheres based on petitRADTRANS is described in Wang et al. (2020; WW20 hereafter). Since low-resolution broad-band data and high-resolution spectroscopic data are used in the retrievals, we consider both resolution modes in petitRADTRANS ($R = 1000$ and $R = 1,000,000$). To sample the posterior distribution in a Bayesian framework, we used PyMultiNest (Buchner et al. 2014), which is based on the MultiNest sampling algorithm (Feroz et al. 2009).

Since petitRADTRANS is the core of our retrieval work, the framework described in this paper can be viewed as an extension of petitRADTRANS. Here, we demonstrate that our framework can analyze data sets that include both high and low spectral-resolution data and that our framework is benchmarked against synthetic and observed spectra.

4.2. Major Updates Since WW20

We list below the updates of our retrieval code since WW20, which make the framework more versatile, flexible, and physical.

4.2.1. Considering High-resolution Spectroscopic Data

In WW20, we excluded the high-res mode in petitRADTRANS for practical reasons. First, computational time was greatly reduced. Second, the highest spectral resolution in our data set was at $R = 5000$ and can be down-sampled to $R = 1000$, which is the low-res mode in petitRADTRANS, without a significant loss of information content. However, our KPIC data has a spectral resolution of $R = 35,000$ and we need to invoke the high-res mode in petitRADTRANS in modeling BD spectra to maximize the information content. In practice, we compute $R = 1,000,000$ modeled spectra in a very narrow spectral range from 2.18 to 2.36 μm , which covers the two spectral orders that we consider. We then downsample the data to match the spectral resolution of KPIC.

Table 3
C and O Abundances for HR 7672 A and Brown Dwarf HR 7672 B

	$\log \epsilon_{\text{C}}$	[C/H]	$\log \epsilon_{\text{O}}$	[O/H]	C/O
HR 7672 A					
This work	8.41 ± 0.05	-0.09 ± 0.05	8.66 ± 0.06	-0.07 ± 0.06	0.56 ± 0.11
da Silva et al. (2015)	8.51 ± 0.03	-0.05 ± 0.03
Brewer et al. (2016)	8.45 ± 0.03	0.06 ± 0.03	8.72 ± 0.04	0.06 ± 0.04	0.53 ± 0.06
Luck (2017)	8.40 ± 0.15	-0.03 ± 0.15	8.63 ± 0.15	-0.06 ± 0.15	0.59 ± 0.10
Solar	8.50 ± 0.06	0.00 ± 0.06	8.73 ± 0.07	0.00 ± 0.07	0.59 ± 0.13
HR 7672 B					
Fixed mass	$8.23^{+0.04}_{-0.04}$	$-0.27^{+0.04}_{-0.04}$	$8.51^{+0.04}_{-0.03}$	$-0.22^{+0.04}_{-0.03}$	$0.52^{+0.02}_{-0.02}$
Free mass	$8.26^{+0.05}_{-0.05}$	$-0.24^{+0.05}_{-0.05}$	$8.54^{+0.04}_{-0.04}$	$-0.19^{+0.04}_{-0.04}$	$0.52^{+0.02}_{-0.02}$

Note. Abundances relative to solar are calculated with respect to the solar values used by each individual paper, which differ from the solar reference used in this work Palme et al. (2014).

4.2.2. Flexible P–T Profile

In WW20, we use an analytical P – T (pressure–temperature) profile (Parmentier & Guillot 2014; Parmentier et al. 2015) to speed up the posterior sampling. However, we find evidence that the analytical P – T profile may not be sufficiently flexible and can bias the retrieved abundances. We therefore switch to a more flexible P – T profile (Piette & Madhusudhan 2020). In the newly adopted P – T profile, there are eight variables including seven temperature differences at eight predefined pressure levels: 100.0, 33.3, 10.0, 3.3, 1.0, 0.1, 0.001, 0.00001 bar. The other variable is the temperature at 3.3 bar.

4.2.3. Physical Cloud Treatment

In WW20, we treated clouds as a gray opaque cloud with infinite opacity if pressures were higher than a certain threshold. In reality, however, this assumption of a gray opaque cloud may be inadequate. Using `petitRADTRANS`, Mollière et al. (2020) adopted a more realistic treatment where silicate and iron clouds were considered. Here, we consider a silicate cloud that only consists of MgSiO_3 for the following reasons. First, it is found that an iron cloud is not as prominent as a silicate cloud (Gao et al. 2020) or the iron cloud is at a much deeper level than the MgSiO_3 cloud (Burningham et al. 2021). Second, considering only MgSiO_3 rather than MgSiO_3 and Mg_2SiO_4 saves computational time, and using both silicate clouds is not expected to provide more meaningful and constraining results compared with a single-cloud model.

In practice, we modify `petitRADTRANS` so that the cloud opacity is included for both low- and high-res modes. To make sure both modes handle cloud opacity consistently, we consider two scenarios for the low-res mode: one with a MgSiO_3 cloud and the other one without a MgSiO_3 cloud (i.e., abundance for MgSiO_3 is set to be zero). We then interpolate the opacity difference of the two scenarios at the central wavelength of the high-res mode. The interpolated opacity is then added in the high-res mode in calculating modeled spectra.

To find the cloud pressure, we intercept the MgSiO_3 condensation curve with the P – T profile. The intercepting pressure marks where the cloud deck is. Then the mass fraction of MgSiO_3 decays exponentially from the cloud deck as controlled by the f_{sed} parameter as discussed in Section 4.3.

4.3. Parameterization

There are 21 parameters in our retrieval code. Three parameters are used to describe the BD properties: surface gravity ($\log(g)$), planet mass (m_p), and the projected rotational velocity ($v \sin i$). Four parameters are for the mass mixing ratio (MMR) of H_2O , CO , CO_2 , and CH_4 . While there exist other species in the atmosphere, they do not significantly alter the spectroscopic and photometric observables. For example, PH_3 has rotation-vibrational features in the K band, but they are much weaker than those from CO and H_2O , even at a MMR that is a few orders of magnitude higher than expected at chemical equilibrium. Both TiO and VO are unaccounted in our model and may affect J -band photometry, but are estimated to be at the 0.1% level, which is much smaller than the photometric uncertainty. Therefore, we focus on four molecular species: H_2O , CO , CO_2 , and CH_4 .

The MMRs are assumed to be constant at all pressures considered. The constant MMRs are justified by the narrow range of pressures that contribute to the thermal flux as well as the nearly constant MMRs for the two major C and O carriers H_2O and CO (see Section 6.6). Moreover, the constant MMR assumption is found to be favored over varying MMR as a function of altitude (Burningham et al. 2021). Eight parameters are for the flexible P – T profile (Section 4.2.2). Similar to Mollière et al. (2020), we use four parameters to describe the cloud properties: MMR of MgSiO_3 , vertical diffusion coefficient (K_{zz}), the ratio of the cloud particle settling and mixing velocities (f_{sed}), and a log-normal particle size distribution parameter (σ_g). The other parameter is for a wavelength shift of the high-resolution spectrum between the data and model.

4.4. Calculating Abundance Ratios

In the K band, CO and H_2O lines are predominately present in the spectrum (Figure 1). Therefore, C and O abundances are mainly constrained by detecting and modeling CO and H_2O lines. For the sake of completeness, we also consider CO_2 and CH_4 in our spectral modeling.

We calculate C/H with the following equation:

$$\text{C/H} = \frac{X_{\text{CO}} + X_{\text{CO}_2} + X_{\text{CH}_4}}{2 \times X_{\text{H}_2} + 4 \times X_{\text{CH}_4} + 2 \times X_{\text{H}_2\text{O}}}, \quad (1)$$

where X is volume mixing ratio (VMR). The conversion from MMR to VMR is given in WW20.

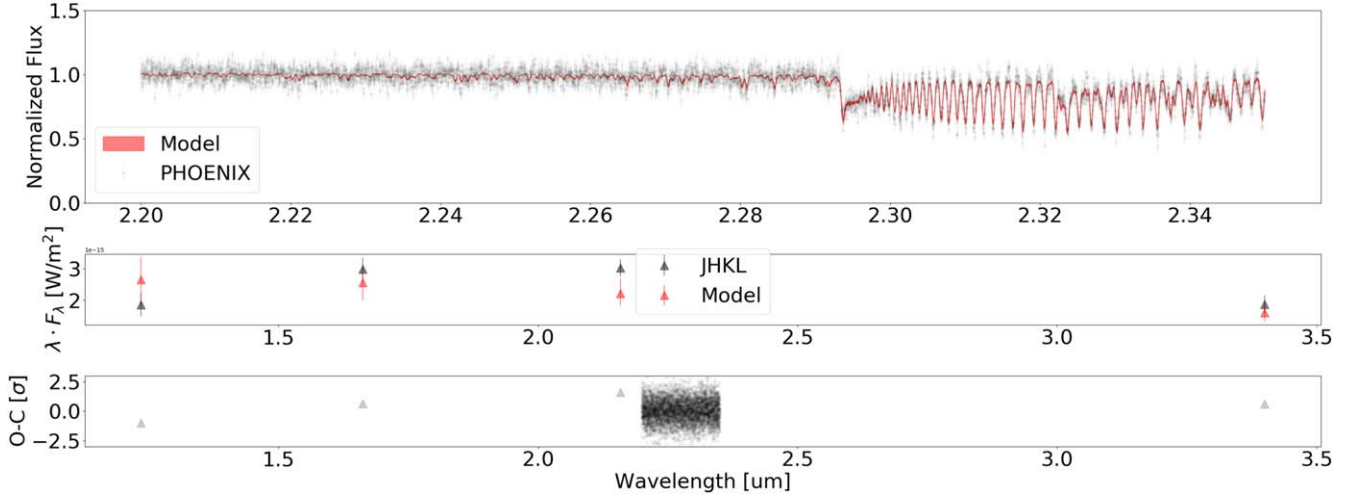


Figure 3. Retrieved spectra based on the PHOENIX spectrum with a Gaussian prior ($72.7 \pm 0.8 M_{\text{Jupiter}}$). Top two panels are simulated high-resolution spectroscopic and photometric data (black) and the modeled data (red). The bottom panel is a residual plot with data minus model and divided by errors.

The MMRs for all considered species add up to unity. The molecular hydrogen to helium ratio is 3:1 from our primordial composition assumption. Similarly, O/H was calculated using the following equation:

$$\text{O/H} = \frac{X_{\text{CO}} + 2 \times X_{\text{CO}_2} + X_{\text{H}_2\text{O}}}{2 \times X_{\text{H}_2} + 4 \times X_{\text{CH}_4} + 2 \times X_{\text{H}_2\text{O}}}. \quad (2)$$

C/O was calculated as:

$$\text{C/O} = \frac{X_{\text{CO}} + X_{\text{CO}_2} + X_{\text{CH}_4}}{X_{\text{CO}} + 2 \times X_{\text{CO}_2} + X_{\text{H}_2\text{O}}}. \quad (3)$$

5. Testing with a PHOENIX BT-Settl Spectrum

Here we test our retrieval framework using a synthetic spectrum for which we know the C and O abundance. The synthetic spectrum is from the PHOENIX BT-Settl model (Baraffe et al. 2015). We choose a synthetic spectrum with T_{eff} of 1600 K, $\log(g)$ of 5.5, and solar abundances.¹⁷ The effective temperature and surface gravity of the synthetic spectrum are similar to those of HR 7672 B.

5.1. Simulating the Data

We obtain wavelength and flux from the PHOENIX spectrum and then scale the flux based on distance and radius. We use a distance of 17.72 pc and a radius of $0.75 R_{\text{Jupiter}}$. The radius is consistent with an object with $\log(g)$ of 5.5 and $72 M_{\text{Jupiter}}$. The fluxes in the *J*, *H*, *K*, and *L* bands are estimated and given the following fractional errors: 0.20, 0.12, 0.09, and 0.15, which are the fractional errors for the actual photometric measurements for HR 7672 B. For fluxes, we use 1.5×10^{-15} , 1.8×10^{-15} , 1.4×10^{-15} , and $5.5 \times 10^{-16} \text{ W } \mu\text{m}^{-1} \text{ m}^{-2}$ for the *J*, *H*, *K*, and *L* bands, respectively.

To simulate high-resolution spectroscopy data, we use a wavelength range from 2.20 to $2.35 \mu\text{m}$. We apply a rotation broadening of 40 km s^{-1} , convolve the spectrum with a Gaussian kernel that corresponds to spectral resolution of $R = 35,000$, and resample the spectrum with a sampling rate of $3 \times 10^{-5} \mu\text{m}$, which translates to approximately two pixels per

resolution element. We add a randomized fractional error of 5% to each data point. The 5% fractional error is comparable to that in the actual HR 7672 B data.

5.2. Retrieval Results

5.2.1. Fixed-mass Case

If the mass is tightly constrained, i.e., a benchmark BD as HR 7672 B with mass measured from the radial velocity technique and the astrometric data, we can apply a Gaussian mass prior. In the fixed-mass case for our PHOENIX retrieval, we apply a Gaussian prior of $72.7 \pm 0.8 M_{\text{Jupiter}}$ for mass and 5.5 ± 0.2 for surface gravity. Our retrieval code can successfully reproduce the high-resolution spectral data and the photometric data (Figure 3). A corner plot of the posterior distribution of all parameters is shown in Figure 14 and the 16th, 50th, and 84th percentiles of the posterior distributions are given in Table 5.

Most importantly, the retrieved C and O abundance distributions encompass the solar values, which are used in the synthetic spectrum (Figure 6). However, the retrieved C/O is overestimated by 0.13 at 0.72 ± 0.03 when compared to the solar value of 0.59. The disagreement is at 4σ , implying potential systematics at the 0.15 level when retrieving C/O. We therefore adopt an uncertainty of 0.15 when reporting C/O values. The adopted uncertainty is also comparable with the C/O uncertainty of the solar C/O at 0.13 (Table 3).

5.2.2. Free-mass Case

We now consider a case with looser priors on mass and surface gravity. Instead of Gaussian priors, we apply a flat prior for mass and surface gravity, i.e., mass between 10 and $100 M_{\text{Jupiter}}$ and $\log(g)$ between 3.5 and 5.5. The upper limit of 5.5 corresponds to the maximum surface gravity for a BD with a contraction time of the age of the universe. We recommend this free-mass prior be applied to most directly imaged planets and BDs for which we do not have a tight mass and surface gravity constraint. In comparison, the informed Gaussian prior in the previous section is recommended for the tests on synthetic spectra and benchmark BDs for which surface gravity is well constrained.

¹⁷ The fits file is available at https://phoenix.ens-lyon.fr/Grids/BT-Settl/CIFIST2011_2015/FITS/.

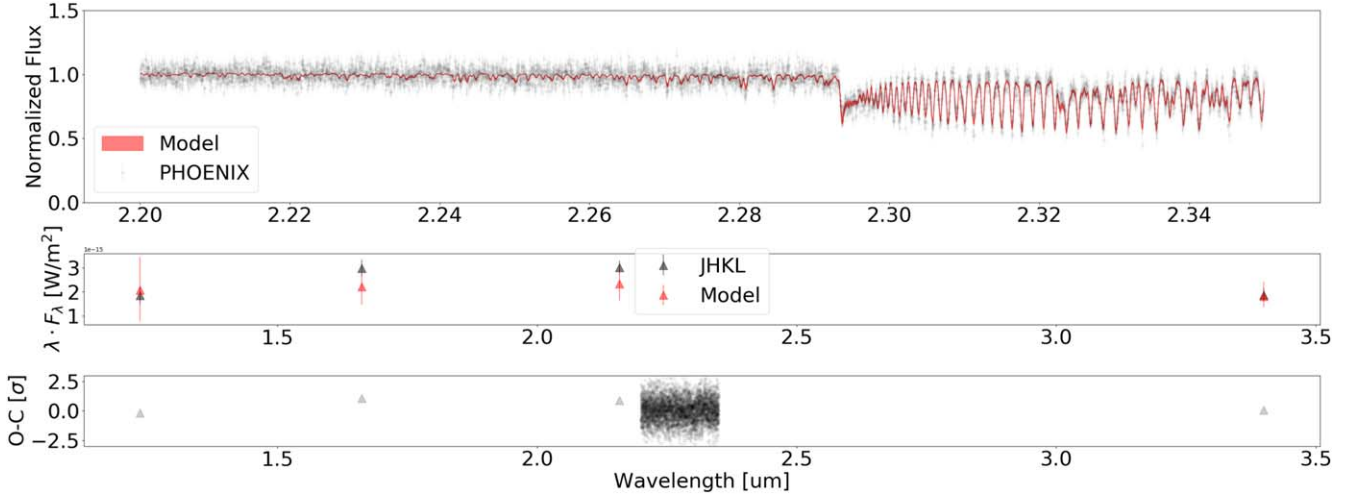


Figure 4. Retrieved spectra based on the PHOENIX spectrum with a flat mass prior between 10 and 100 M_{Jupiter} . The top two panels are simulated high-resolution spectroscopic and photometric data (black) and the modeled data (red). The bottom panel is a residual plot with data minus model and divided by errors.

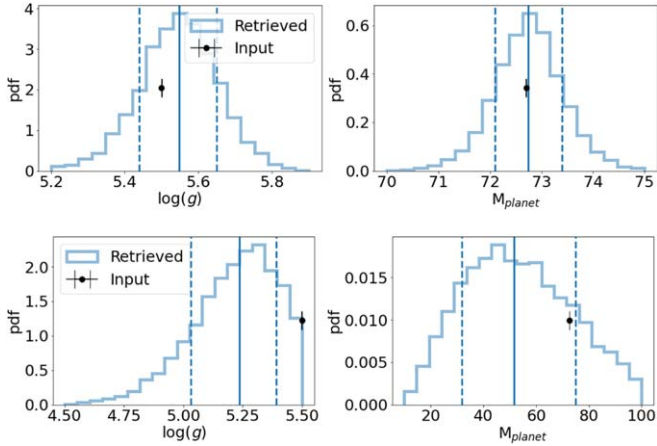


Figure 5. Retrieved surface gravity and mass based on the PHOENIX spectrum. Comparing surface gravity and mass from posterior samples (blue histograms) to PHOENIX input values (black data points) shows an agreement within 1σ for, top, a Gaussian prior ($72.7 \pm 0.8 M_{\text{Jupiter}}$), and $1-2\sigma$ agreement for, bottom, a flat mass prior between 10 and 100 M_{Jupiter} . Vertical lines mark the 16th, 50th, and 84th percentiles of posterior samples.

While we can successfully reproduce the high-resolution spectral data and the photometric data (Figure 4), the retrieved $\log(g)$ and mass are lower than input values by $\sim 1-2\sigma$ as shown in Table 5 and Figure 5. A complete corner plot is shown in Figure 15. This may indicate that the high-resolution spectroscopic data and the photometric data points alone do not put a tight constraint on mass and surface gravity.

The retrieved C and O abundances agree well with the solar values as shown in Figure 6. The retrieved C/O is overestimated by 0.18 at 0.77 ± 0.04 when compared to the solar value of 0.59. This is again a $\sim 4\sigma$ discrepancy given the formal error bar from the retrieval analysis. If using the 0.15 adopted C/O uncertainty as discussed in the previous section, this is a 1.2σ discrepancy.

Figure 7 shows a number of pressure-dependent properties. First, the 1σ uncertainty region of the retrieved $P-T$ profile is marked in red. When intercepting the condensation temperature of MgSiO_3 (~ 1700 K, Marley et al. 2013), the blue dotted line indicates the pressure level where MgSiO_3 clouds form. This is consistent (by design, see Section 4.2.3) with the retrieved

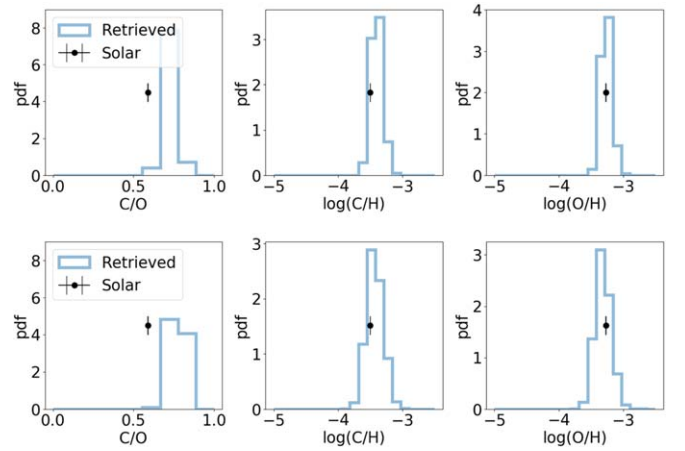


Figure 6. Retrieved C and O abundances and C/O based on the PHOENIX spectrum. While C and O abundances from posterior samples (blue histograms) agree well with the solar values (black data points), the retrieved C/O is consistently higher than the solar C/O. Top: with a Gaussian prior ($72.7 \pm 0.8 M_{\text{Jupiter}}$). Bottom: with a flat mass prior between 10 and 100 M_{Jupiter} .

properties of the MgSiO_3 cloud whose opacity distribution is shown as the black dashed line.

The contribution function (black solid line in Figure 7) coincides with the cloud opacity, indicating a cloudy condition. However, a closer look at the cloud opacity reveals that the cloud contributes negligible optical depth. The retrieved cloud opacity is $\sim 10^{-6} \text{ g cm}^{-2}$. At a pressure of 3 bar and a temperature of 1500 K, where the cloud opacity peaks, the density is $5.5 \times 10^{-5} \text{ g cm}^{-3}$ assuming an ideal gas law with a mean molecular weight of 2.3. Based on $\tau = \kappa \rho l$, where τ is optical depth, κ is opacity, and l is the atmosphere thickness, the optical depth is 0.005 even if we assume a thickness of 1000 km.

In comparison, the cloudy condition is predicted by the BT-Settl model (e.g., Figure 4 in Allard et al. 2012) at an effective temperature of 1600 K. The discrepancy can be reconciled by the higher surface gravity (by 0.5 dex) that we consider here. At a higher surface gravity, the cloud deck sinks and therefore reveals a cloudless condition.

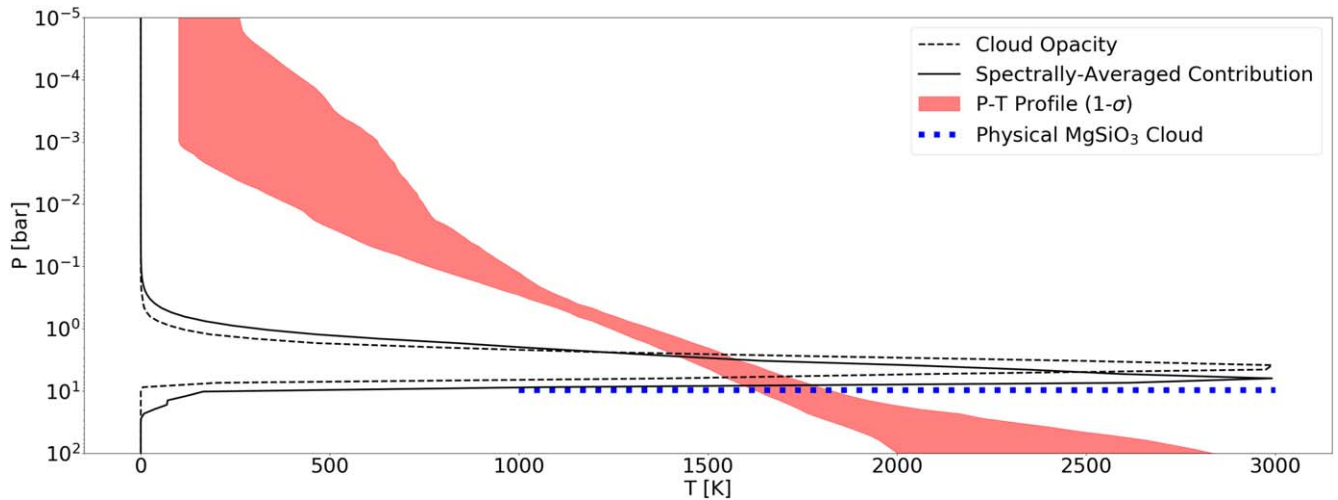


Figure 7. Retrieved P - T profile (1σ region in red shaded region) based on the PHOENIX spectrum. The spectrally averaged contribution function is shown as the black solid line, which overlaps with the retrieved cloud layer (black dashed line). The cloud opacity does not significantly contribute to the emission because the optical depth of the cloud is small (Section 5.2.2). The pressure level of the retrieved cloud layer is consistent with that of a physical MgSiO_3 cloud (blue dotted line).

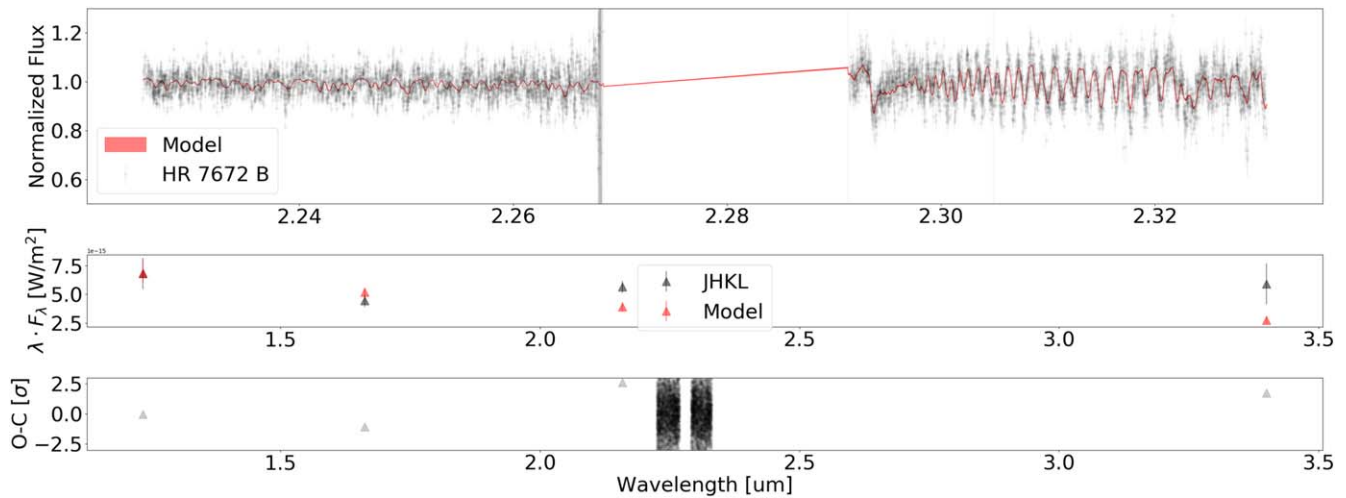


Figure 8. Retrieved spectra for HR 7672 B with a Gaussian prior ($72.7 \pm 0.8 M_{\text{Jupiter}}$). The top two panels are simulated high-resolution spectroscopic and photometric data (black) and the modeled data (red). The bottom panel is a residual plot with data minus model and divided by errors.

5.3. Potential Reasons for Overestimating C/O

There may be a few caveats that lead to biases in estimating C/O. First, spectral normalization can affect C and O detection and retrieved abundances (Rasmussen et al. 2021). In particular, in the presence of noise, the CO band-head strength is likely to be underestimated as a result of spectral normalization. However, a reduced CO band-head strength will lead to a lower C abundance, and therefore a lower C/O, which is the opposite to our result.

Second, the P - T profile can affect C/O measurements. As shown in Wang et al. (2020), a difference in parameterizing the P - T profile leads to significantly different C/O measurements. This motivates the more flexible P - T profile used in this work, so we conclude that the P - T profile is less likely to cause the C/O overestimation.

Third, line saturation can bias C and O measurements. In K -band spectroscopy, CO lines tend to be deeper and H_2O tend to be weaker (Figure 1). Deep versus saturated CO lines are less distinguishable in high-resolution retrieval after continuum normalization. This can lead to an overestimation of C abundance, which is consistent with our findings of the

retrieval on the synthetic spectrum. A similar result is also found in Finnerty et al. (2021) where overestimation of C/O is reported in retrievals for spectra with C/O lower than 0.5, although the bias in measuring C/O is smaller than 0.1.

Last, weak H_2O lines tend to be interpreted as noise in the spectrum. This leads to an underestimation of O abundance and therefore a bias for a higher C/O, which is another plausible explanation for the higher C/O than solar value that is retrieved for the synthetic spectrum.

In conclusion, the above exercise with a PHOENIX synthetic spectrum (1) tests the limits (e.g., retrieving mass and surface gravity) and estimates a more practical error bar (e.g., measuring C/O) and (2) validates our framework so that we can use it to retrieve C and O abundances based on the actual HR 7672 B data set.

6. Retrieving Properties for HR 7672 B

6.1. Data versus Modeled Spectra

We use our retrieval framework to infer atmospheric C and O abundance for HR 7672 B using a data set that combines

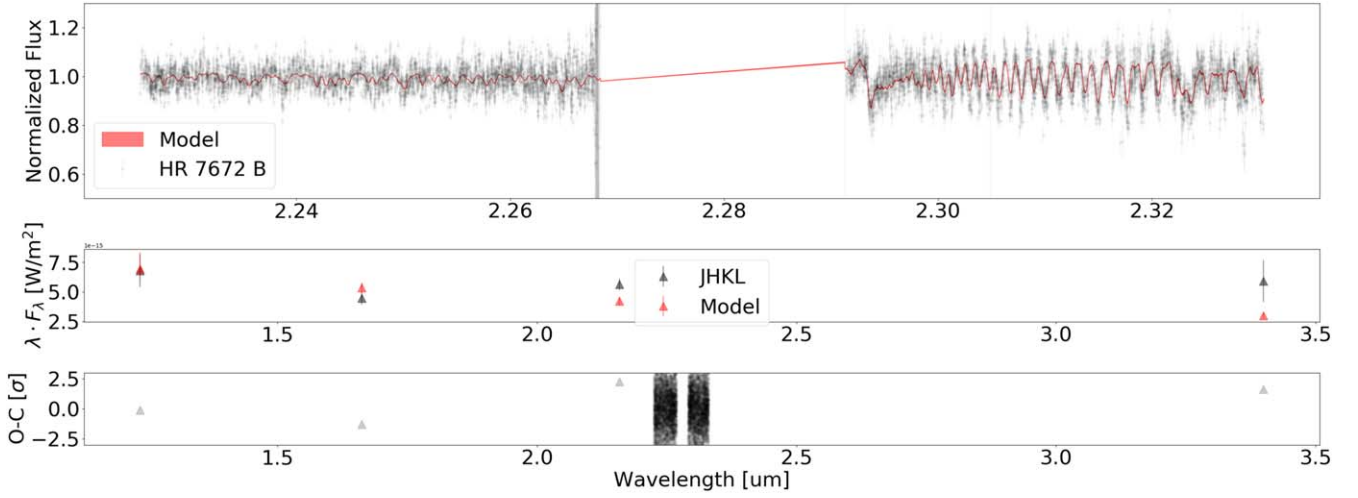


Figure 9. Retrieved spectra for HR 7672 B with a flat mass prior between 10 and 100 M_{Jupiter} . The top two panels are simulated high-resolution spectroscopic and photometric data (black) and the modeled data (red). The bottom panel is a residual plot with data minus model and divided by errors.

Table 4
Parameters Used in Retrieval and their Priors

Parameter	Unit	Type	Lower or Mean	Upper or Std
Fixed surface gravity ($\log(g)$)	cgs	Gaussian	5.5	0.2
Free surface gravity ($\log(g)$)	cgs	Uniform	3.5	5.5
Fixed mass (M_P)	M_{Jupiter}	Gaussian	72.7	0.8
Free mass (M_P)	M_{Jupiter}	Uniform	10	100
H ₂ O mixing ratio ($\log(mr_{\text{H}_2\text{O}})$)	...	Log-uniform	-10	-1
CO mixing ratio ($\log(mr_{\text{CO}})$)	...	Log-uniform	-10	-1
CO ₂ mixing ratio ($\log(mr_{\text{CO}_2})$)	...	Log-uniform	-10	-1
CH ₄ mixing ratio ($\log(mr_{\text{CH}_4})$)	...	Log-uniform	-10	-1
Temperature at 3.2 bar (t_{int})	K	Uniform	1000	2000
ΔT between 100 and 32 bar	K	Uniform	0	2500
ΔT between 32 and 10 bar	K	Uniform	0	2000
ΔT between 10 and 3.2 bar	K	Uniform	0	1500
ΔT between 3.2 and 1 bar	K	Uniform	0	1000
ΔT between 1 and 0.1 bar	K	Uniform	0	1000
ΔT between 0.1 bar and 1 mbar	K	Uniform	0	1000
ΔT between 1 mbar and 10 nbar	K	Uniform	0	1000
MgSiO ₃ mixing ratio ($\log(mr_{\text{MgSiO}_3})$)	...	Log-uniform	-10	-2
Vertical diffusion coefficient ($\log(K_{zz})$)	$\text{cm}^2 \text{s}^{-1}$	Log-uniform	5	10
$v_{\text{settling}}/v_{\text{mixing}} (f_{\text{sed}})$...	Uniform	0	5
Width of log-normal particle size distribution (σ_g)	...	Uniform	1.05	3.05
Wavelength shift (Δ_λ)	μm	Uniform	-0.01	0.01
y offset (Δ_y)	...	Uniform	-0.1	0.1
Rotational blurring (f_{blur})	km s^{-1}	Uniform	2	100

high-resolution data from KPIC and photometric data as detailed in Section 2. The retrieval setup was the same as our tests using the PHOENIX synthetic spectrum, except for one additional free parameter that accounts for the normalized flux offset between the high-resolution data and the modeled spectrum. This free parameter is introduced because of the uncertainty of normalizing the observed spectrum in the presence of noises.

Similar to Section 5, we consider two cases: the fixed-mass case and the free-mass case. The fixed-mass case is for retrieving objects with tight mass constraints. The free-mass case is for the majority of directly imaged planets and BDs without tight mass constraints. Figures 8 and 9 show the comparison between data and models using posterior samples (Figures 16 and 17). In both cases, spectral models from

posterior samples agree well with the observed spectrum and photometric data points except for the *K*- and *L*-band photometry, which shows $\sim 2\text{--}3\sigma$ discrepancy. The discrepancy can be attributed to a degeneracy in retrieving clouds and is discussed in Sections 6.4 and 6.5.

Despite the $\sim 2\text{--}3\sigma$ discrepancy for the *K*- and *L*-band photometry, the retrieved luminosity for HR 7672 B ($\log(L_{\text{bol}}/L_\odot) = -4.08 \pm 0.06$) agrees with literature values within $\sim 1\sigma$, e.g., $\log(L_{\text{bol}}/L_\odot) = -4.19 \pm 0.04$ (Brandt et al. 2019) and $\log(L_{\text{bol}}/L_\odot) = -4.12 \pm 0.09$ (Liu et al. 2002). The retrieved effective temperature (1806 ± 77 K) also falls in the previously estimated range between 1510 and 1850 K (Liu et al. 2002).

We also note that HR 7672 B is a very fast rotator with a $v \sin i$ of $45.0 \pm 0.5 \text{ km s}^{-1}$, potentially making it an excellent

Table 5
Summary of Retrieval Results

Parameter	Unit	PHOENIX		HR 7672 B	
		Fixed	Free	Fixed	Free
Mass					
$\log(g)$	cgs	$5.55^{+0.10}_{-0.11}$	$5.24^{+0.16}_{-0.20}$	$5.40^{+0.08}_{-0.06}$	$5.44^{+0.04}_{-0.07}$
M_P	M_{Jupiter}	$72.74^{+0.66}_{-0.64}$	$51.70^{+23.26}_{-19.73}$	$72.84^{+0.71}_{-0.72}$	$89.97^{+6.86}_{-11.18}$
$\log(mr_{\text{H}_2\text{O}})$...	$-2.72^{+0.08}_{-0.08}$	$-2.86^{+0.12}_{-0.12}$	$-2.69^{+0.03}_{-0.03}$	$-2.66^{+0.03}_{-0.04}$
$\log(mr_{\text{CO}})$...	$-2.10^{+0.09}_{-0.08}$	$-2.13^{+0.13}_{-0.12}$	$-2.46^{+0.04}_{-0.04}$	$-2.43^{+0.05}_{-0.05}$
$\log(mr_{\text{CO}_2})$...	$-6.37^{+2.30}_{-2.18}$	$-6.21^{+2.25}_{-2.25}$	$-6.40^{+2.37}_{-2.30}$	$-6.45^{+2.33}_{-2.29}$
$\log(mr_{\text{CH}_4})$...	$-7.19^{+1.60}_{-1.66}$	$-7.10^{+1.61}_{-1.69}$	$-8.07^{+1.26}_{-1.22}$	$-7.97^{+1.31}_{-1.29}$
t_{int}	K	$1627.88^{+93.33}_{-102.34}$	$1534.06^{+95.46}_{-92.77}$	$1530.81^{+48.28}_{-28.15}$	$1528.32^{+41.95}_{-29.13}$
ΔT between 100 and 32 bar	K	$258.72^{+247.87}_{-172.03}$	$548.00^{+658.13}_{-359.59}$	$307.00^{+314.60}_{-210.94}$	$317.98^{+326.28}_{-219.23}$
ΔT between 32 and 10 bar	K	$103.68^{+103.15}_{-69.98}$	$210.50^{+239.61}_{-141.82}$	$235.43^{+188.47}_{-140.30}$	$204.66^{+174.18}_{-127.16}$
ΔT between 10 and 3.2 bar	K	$111.52^{+102.02}_{-72.21}$	$141.11^{+118.29}_{-89.29}$	$333.62^{+66.59}_{-100.92}$	$311.36^{+67.24}_{-95.21}$
ΔT between 3.2 and 1 bar	K	$391.81^{+164.72}_{-156.98}$	$214.36^{+136.42}_{-118.49}$	$27.06^{+38.12}_{-19.32}$	$33.20^{+43.91}_{-23.68}$
ΔT between 1 and 0.1 bar	K	$498.01^{+248.72}_{-243.04}$	$482.01^{+232.47}_{-219.63}$	$18.52^{+40.72}_{-13.86}$	$20.90^{+34.02}_{-15.29}$
ΔT between 0.1 bar and 1 mbar	K	$485.32^{+299.40}_{-289.41}$	$496.15^{+283.12}_{-287.49}$	$871.08^{+89.54}_{-143.57}$	$828.82^{+117.63}_{-179.88}$
ΔT between 1 mbar and 10 nbar	K	$510.73^{+286.06}_{-297.90}$	$504.10^{+287.28}_{-283.59}$	$337.96^{+360.25}_{-239.78}$	$396.66^{+359.62}_{-278.23}$
$\log(mr_{\text{MgSiO}_3})$...	$-6.47^{+2.03}_{-2.12}$	$-4.75^{+1.73}_{-2.86}$	$-6.96^{+1.89}_{-1.91}$	$-6.50^{+1.97}_{-2.22}$
$\log(K_{zz})$	$\text{cm}^2 \text{s}^{-1}$	$7.60^{+1.41}_{-1.49}$	$7.59^{+1.48}_{-1.48}$	$7.65^{+1.52}_{-1.67}$	$7.62^{+1.56}_{-1.69}$
f_{sed}	...	$2.54^{+1.43}_{-1.45}$	$2.86^{+1.51}_{-1.51}$	$2.52^{+1.56}_{-1.57}$	$2.56^{+1.57}_{-1.60}$
σ_g	...	$2.04^{+0.58}_{-0.57}$	$2.03^{+0.61}_{-0.57}$	$2.04^{+0.64}_{-0.64}$	$2.03^{+0.65}_{-0.63}$
Δ_λ	μm	$0.00^{+0.00}_{-0.00}$	$0.00^{+0.00}_{-0.00}$	$0.00^{+0.00}_{-0.00}$	$0.00^{+0.00}_{-0.00}$
Δ_y	$0.08^{+0.00}_{-0.00}$	$0.08^{+0.00}_{-0.00}$
f_{blur}	km s^{-1}	$39.62^{+1.40}_{-1.39}$	$38.71^{+1.67}_{-1.84}$	$45.03^{+0.45}_{-0.43}$	$45.04^{+0.55}_{-0.53}$
[C/H]	dex	$0.09^{+0.9}_{-0.08}$	$0.06^{+0.13}_{-0.11}$	$-0.27^{+0.04}_{-0.04}$	$-0.24^{+0.05}_{-0.05}$
[O/H]	dex	$0.00^{+0.08}_{-0.07}$	$-0.05^{+0.12}_{-0.11}$	$-0.22^{+0.04}_{-0.03}$	$-0.19^{+0.04}_{-0.04}$
C/O	...	$0.72^{+0.03}_{-0.03}$	$0.77^{+0.04}_{-0.04}$	$0.52^{+0.02}_{-0.02}$	$0.52^{+0.02}_{-0.02}$

Note. (a) We report the median of posterior distribution and error bars correspond to the difference of the median and the 68% credible interval. (b) We adopt solar elemental abundances from Palme et al. (2014).

object for Doppler imaging. Our $v \sin i$ is 1.8σ off the measurement by Delorme et al. (2021) at $42.6 \pm 0.8 \text{ km s}^{-1}$.

6.2. Fixed Mass versus Free Mass

The mass of HR 7672 B is well constrained because of available radial velocity data and astrometric data (Crepp et al. 2012; Brandt et al. 2019). This corresponds to the fixed-mass case. However, we would like to investigate a case in which tight constraints are not available. This corresponds to the free-mass case, in which we set a flat prior for mass and surface gravity (see Table 4).

For the fixed-mass case, the retrieved surface gravity and mass posteriors agree well with measured values (Figure 10 top and Table 5). The mass constraints are from radial velocity and astrometric data (Brandt et al. 2019). The surface gravity constraints are from the age measurement of $\sim 2\text{--}4$ Gyr (Brandt et al. 2019) and BD evolutionary models (Saumon & Marley 2008). Assuming the HR 7672 system has an age of between 2 and 4 Gyr (Brandt et al. 2019), the $\log(g)$ of HR 7672 B should be between 5.33 and 5.35 based on Saumon & Marley (2008) and surely lower than 5.50. For the free-mass case (Figure 10 bottom), while the retrieved surface gravity agrees with the Saumon & Marley (2008) measured value, the mass posteriors differ by $1\text{--}2\sigma$. The $1\text{--}2\sigma$ difference is consistent with our findings using the PHOENIX synthetic spectrum.

The comparison between the fixed-mass case and the free-mass case shows that our retrieval framework can retrieve mass and surface gravity within $1\text{--}2\sigma$ for BDs like HR 7672 B. Further tests are needed for directly imaged exoplanets with lower surface gravity.

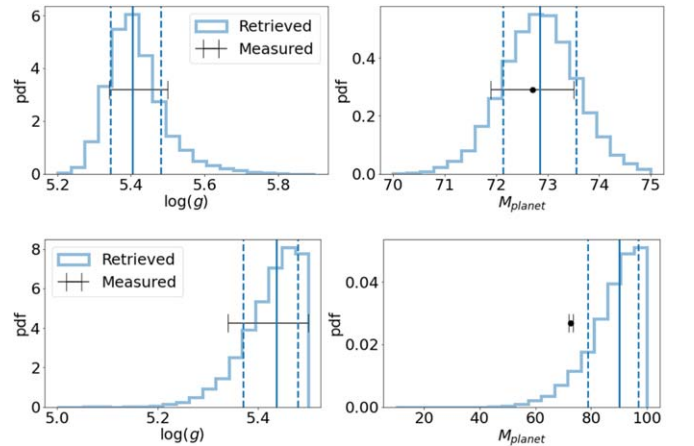


Figure 10. Retrieved surface gravity and mass for HR 7672 B. Top with a Gaussian prior ($72.7 \pm 0.8 M_{\text{Jupiter}}$): retrieved surface gravity and mass (blue histograms) agree well with measured values (black data points with error bars). Bottom with a flat mass prior between 10 and $100 M_{\text{Jupiter}}$: while the retrieved surface gravity agrees with the measured value, the mass posteriors differ by $1\text{--}2\sigma$. Vertical lines mark the 16th, 50th, and 84th percentiles of posterior samples.

6.3. C/O

Moreover, the retrieved C and O abundances and C/O for HR 7672 B agree within $1\text{--}2\sigma$ with those of HR 7672 A (Figure 11). Consistency is seen for both the fixed-mass case and the free-mass case. Using the free-mass case as an example, the retrieved

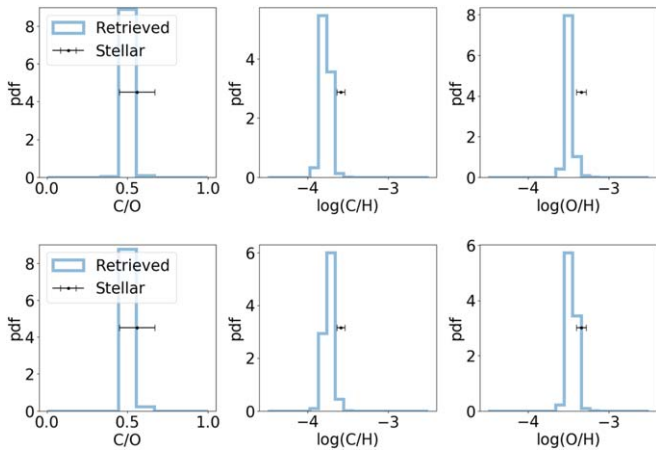


Figure 11. Retrieved C and O abundances and C/O for HR 7672 B. Comparing C/O, C/H, and O/H from posterior samples (blue histograms) to stellar values (black data points with error bars) shows an agreement within $1-2\sigma$. Top: with a Gaussian prior ($72.7 \pm 0.8 M_{\text{Jupiter}}$). Bottom: with a flat mass prior between 10 and $100 M_{\text{Jupiter}}$.

[C/H], [O/H], and C/O are below stellar values by 1.5σ , 1.2σ , and 0.3σ , respectively. From previous work on benchmark BDs, $<2\sigma$ difference is considered to be in good agreement (Line et al. 2015).

We also note that the retrieved uncertainties for [C/H], [O/H], and C/O are likely underestimated. This is not uncommon in recent papers that perform retrieval analyses on directly imaged exoplanets and brown dwarfs. For example, reported C/O uncertainty is 0.06–0.07 in Mollière et al. (2020) and Burningham et al. (2021), much lower than the solar C/O uncertainty at 0.13 (Palme et al. 2014). Additional unaccounted-for systematic errors can exceed the formal uncertainties. This is evidenced by the C/O discrepancy as seen in Section 5.2.2 for the PHOENIX retrieval and possible explanations are discussed in Section 5.3.

Moreover, surface inhomogeneity (Crossfield et al. 2014) and time variability (Karlidi et al. 2016) would contribute to C/O uncertainty. This is because the 3D time-varying surface features cannot be adequately addressed by the 1D modeling code that we use in this work. Also, small wavelength coverage in high spectral resolution data may also contribute to the additional unknown systematics, which can be mitigated by increased spectral grasp.

In addition, there is a subtle difference between atmospheric abundance and intrinsic abundance as pointed out by Line et al. (2015). The atmospheric abundance is retrieved based on the BD spectrum and the intrinsic abundance is measured based on the primary star. The latter is intrinsic because of efficient mixing in the photosphere of the primary star. The atmospheric abundance from a BD can be affected by condensation, which will decrease oxygen abundance because a condensed particle is likely to contain oxygen, e.g., MgSiO_3 . However, our retrieved MgSiO_3 abundance is at lower than 10^{-4} level. Therefore, the oxygen locked in MgSiO_3 will not significantly affect the retrieved O/H and C/O when comparing the MgSiO_3 abundance to the major O carrier H_2O and CO for which the abundance is at 10^{-3} – 10^{-2} level.

6.4. Cloud Property and Degeneracy

Figure 12 shows the retrieved P – T profile as well as the contribution function. Similarly to the PHOENIX retrieval case, we infer a cloudless condition even though the cloud

opacity peaks roughly near the peak of the contribution function. This is because the optical depth due to the cloud is negligible given the low opacity value that is smaller than $10^{-5} \text{ g cm}^{-2}$. Moreover, cloud properties are mostly unconstrained as shown in Figures 16 and 17.

The inferred cloudless condition may be due to a degeneracy as discussed in Tremblin et al. (2017): the existence of clouds can be masqueraded by a decrease of thermal gradient of the P – T profile. Both clouds and a nearly isothermal P – T profile can lead to shallower absorption lines. The isothermal knee around 1 bar in our retrieved P – T profile is the evidence of this degeneracy. Similar effects are also discussed in Mollière et al. (2020). Therefore, we do not know if the inferred cloudless condition is real or due to an artificially isothermal P – T profile.

One solution to break the degeneracy is to use a self-consistent P – T profile as done in Mollière et al. (2020). However, a self-consistent P – T profile may not necessarily be the actual P – T profile in the BD atmosphere. Therefore, future James Webb Space Telescope data will play a key role in resolving this degeneracy (Tremblin et al. 2017).

6.5. Fainter Retrieved K- and L-band Photometry Than Observation

The degeneracy under discussion here may also explain the 2–3 σ discrepancy of K - and L -band photometry that is seen in the retrieval for HR 7672 B (see Figures 8 and 9). While the MultiNest sampling algorithm preferentially finds the cloudless solution for the reason that is detailed in the next paragraph, an alternative cloudy solution can tilt the spectral energy distribution of the J , H , K , and L bands, namely, making the J and H bands dimmer while leaving the K and L bands relatively unchanged. This is because clouds affect shorter wavelengths more than longer wavelengths. In this way, all four modeled photometric data points are consistently below the actual measurement points. Thus, to account for the overall fainter modeled photometry than the observation, the retrieved radius is inflated in the retrieval and therefore results in a lower surface gravity.

The reason why the retrieval favors the cloudless solution is that the weight for photometric data points is small: there are only four photometric data points whereas there are over 7000 spectroscopic data points. It is expected that, when the weight of photometric data points increases, the discrepancy of photometry is reduced. Indeed, this is what happens when increasing the photometric weight by adding redundant photometric data points that repeat themselves. However, the retrieved surface gravity becomes too low to be realistic. This delicate issue will be discussed in more detail in a forthcoming paper.

6.6. Chemical Equilibrium?

We investigate the agreement between our retrieved abundances and those expected from chemical equilibrium. The comparison helps to check if reasonable abundances are retrieved.

We use `poor_mans_nonequ_chem` to interpolate a pre-calculated chemical grid from `easyCHEM` (Mollière et al. 2017). The grid spans multiple dimensions including temperature (60–4000 K), pressure (10^{-8} –1000 bar), C/O (0.1–1.6), and [Fe/H] (–2–3). To calculate the equilibrium abundance, we use the median of the retrieved P – T profile and stellar values of C/O = 0.56 and [Fe/H] = –0.04. While the uncertainties of the

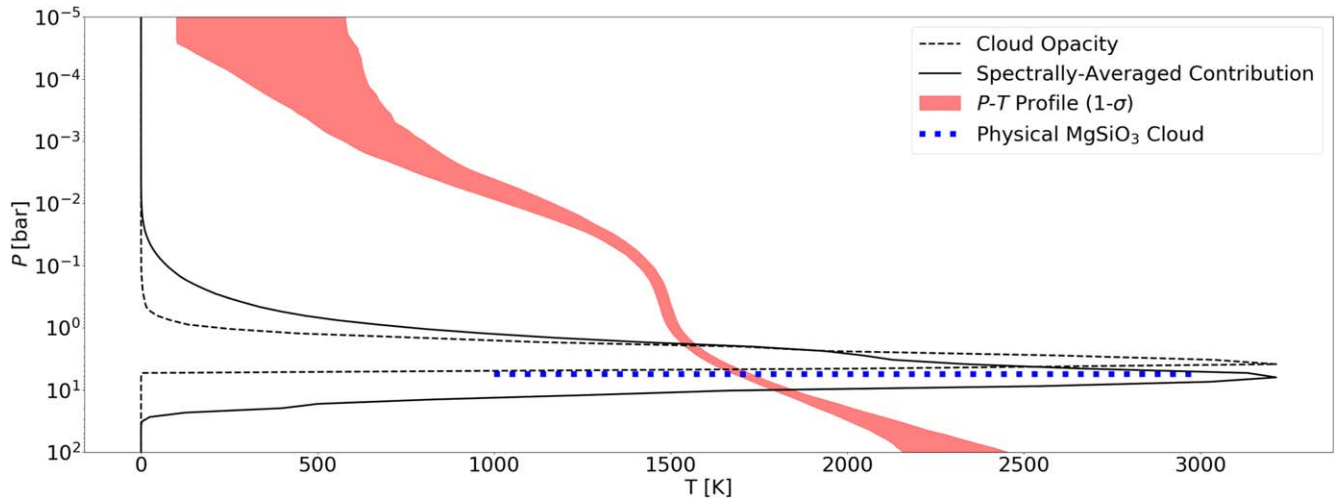


Figure 12. Retrieved P - T profile (1σ region in red shaded region) for HR 7672 B. The spectrally averaged contribution function is shown as the black solid line, which overlaps with retrieved cloud layer (black dashed line). The cloud opacity does not significantly contribute to the emission because the optical depth of the cloud is small (see Section 6.4). The pressure level of the retrieved cloud layer is consistent with that of a physical MgSiO_3 cloud (blue dotted line). The isothermal knee of the P - T profile between 0.1 and 1 bar may be responsible for the cloudless inference. The degeneracy between a cloudy atmosphere and a cloudless atmosphere with a reduced thermal gradient (e.g., the isothermal knee) in the P - T profile is discussed in Section 6.4.

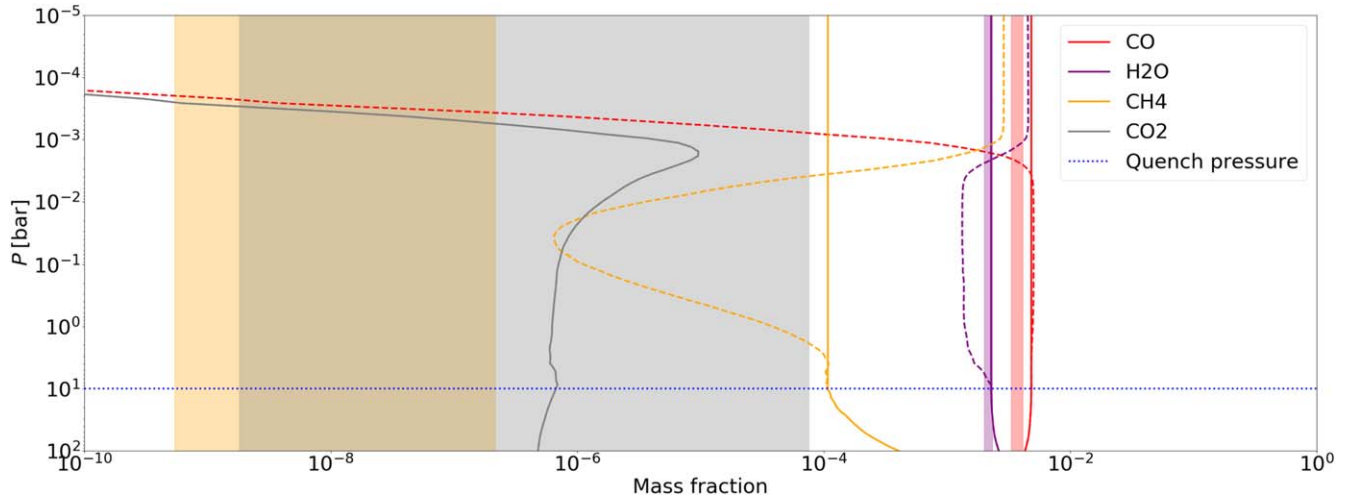


Figure 13. Abundances assuming equilibrium chemistry (solid) and a quenched pressure at 10 bar (dashed). 1σ ranges of retrieved abundances are shown in shaded regions. The expected CO and H_2O abundances are much higher than those of CO_2 and CH_4 , so CO and H_2O are two dominant C and O carriers. This is consistent with detected CO and H_2O lines in K -band spectroscopy (Figure 1).

P - T profile, C/O, and $[\text{Fe}/\text{H}]$ all contribute to the uncertainty of the equilibrium abundance, we show below that the adopted values for the chemical grid result in reasonable agreement with the retrieved abundance.

Figure 13 shows the abundances (in mass mixing ratio) for four species (CO, H_2O , CH_4 , and CO_2) assuming two conditions: chemical equilibrium, and a quenched case of chemical disequilibrium, where vertical mixing homogenizes abundances above a quench pressure which we set at 10 bar.

For the two constrained species (CO and H_2O), the H_2O abundance agrees well with the quenched condition, but the retrieved CO abundance is below the value as interpolated from the chemical grid (by $\sim 1\sigma$). The difference can be reconciled by varying the quench pressure, the P - T profile, C/O, and $[\text{Fe}/\text{H}]$ values that are within the posterior range. A more rigorous approach would be to sample the posterior and infer a range of possible values from the chemical grid.

For the two unconstrained species (CH_4 and CO_2), the 16%–85% credible range for CO_2 agrees well with both the chemical

equilibrium and the quenched conditions. However, the retrieved CH_4 abundance range is well below the value as expected from the chemical grid.

7. Summary

This paper has the goal of measuring chemical composition to better understand the origin of substellar companions. First, we measure stellar abundance for HR 7672 A using archival data from the Keck Observatory Archive. The resulting stellar parameters and abundance for C and O are reported in Tables 2 and 3, which are in $<2\sigma$ agreement with previous measurements.

Second, using KPIC, we obtain high-resolution ($R = 35,000$) data for HR 7672 B, a benchmark BD around HR 7672 A. We measure L -band photometry for HR 7672 B using Keck NIRC2 archival data. Along with previous J -, H -, and K -band photometric data points, the spectrum and photometric data points are used to validate a retrieval framework, which is an extension of `petitRADTRANS`. We show that the framework

can retrieve correctly the C and O abundances that are used in a synthetic PHOENIX BT-Settl spectrum (Section 5). However, the retrieved C/O is overestimated by 0.13–0.18 (4σ) using the formal uncertainty from the retrieval. We therefore recommend a 0.15 uncertainty for the retrieved C/O. We also show that our retrieval framework can retrieve C and O abundances and C/O from a benchmark BD HR 7672 B that are within 1.5σ consistent with the primary star HR 7672 A (Section 6).

The work presented here provides a practical procedure of testing and performing atmospheric retrieval on data sets that span a large range of spectral resolution (e.g., from photometric data to R of 35,000) and wavelength coverage (J through L band). Our exercises on a synthetic spectrum and the HR 7672 B data set enable us to understand the limitations and uncertainties in retrieving BD properties and lend confidence in using the framework on future data sets from more BDs and exoplanets.

We thank the anonymous referee whose comments and suggestions significantly improve the paper. We would like to thank Paul Molliere for the help in setting up and running `petitRADTRANS`. We thank Anjali Piette for helpful discussion on the P – T profile. We thank the Heising-Simons Foundation for supporting the workshop on combining high-resolution spectroscopy and high-contrast imaging for

exoplanet characterization, where the idea originated of combining photometric data and spectral data of different resolutions. KPIC has been supported by the Heising-Simons Foundation through grants #2015-129, #2017-318, and #2019-1312. This work was also partially supported by the Simons Foundation. The data presented herein were obtained at the W. M. Keck Observatory, which is operated as a scientific partnership among the California Institute of Technology, the University of California and the National Aeronautics and Space Administration. The Observatory was made possible by the generous financial support of the W. M. Keck Foundation. The authors wish to recognize and acknowledge the very significant cultural role and reverence that the summit of Maunakea has always had within the indigenous Hawaiian community. We are most fortunate to have the opportunity to conduct observations from this mountain.

Appendix Corner Plots for Retrievals

We provide the corner plots of posteriors in our retrieval analyses, including the fixed-mass case (Figure 14) and the free-mass case (Figure 15) for the PHOENIX retrieval, and the fixed-mass case (Figure 16) and the free-mass case (Figure 17) for the HR 7672 B retrieval.

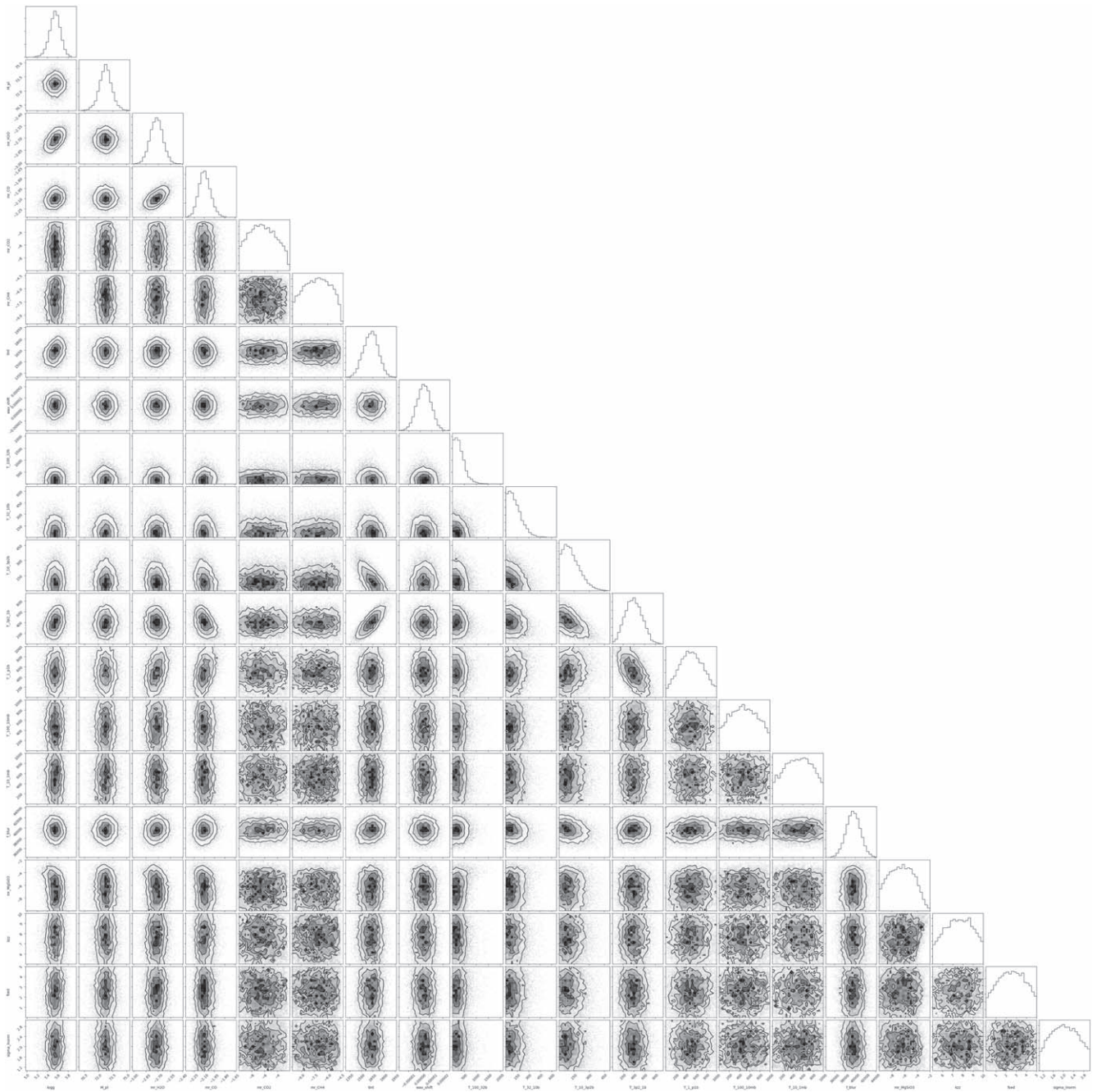


Figure 14. Posterior distributions for the PHOENIX retrieval by fixing the mass to $72.7 \pm 0.8 M_{\text{Jupiter}}$ (see Section 5).

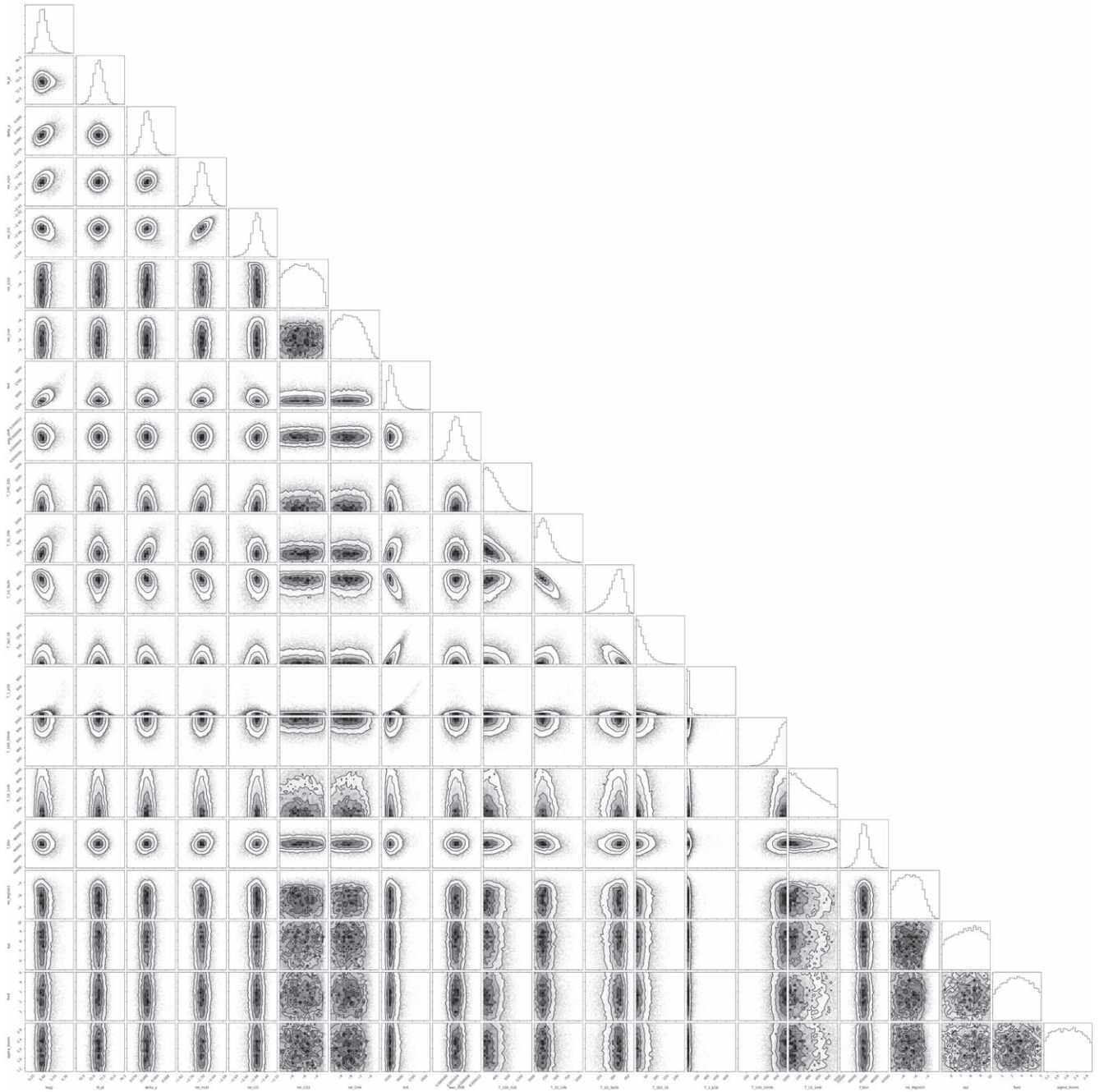


Figure 16. Posterior distributions for the retrieval for HR 7672 B by fixing the mass to $72.7 \pm 0.8 M_{\text{Jupiter}}$ (see Section 6).

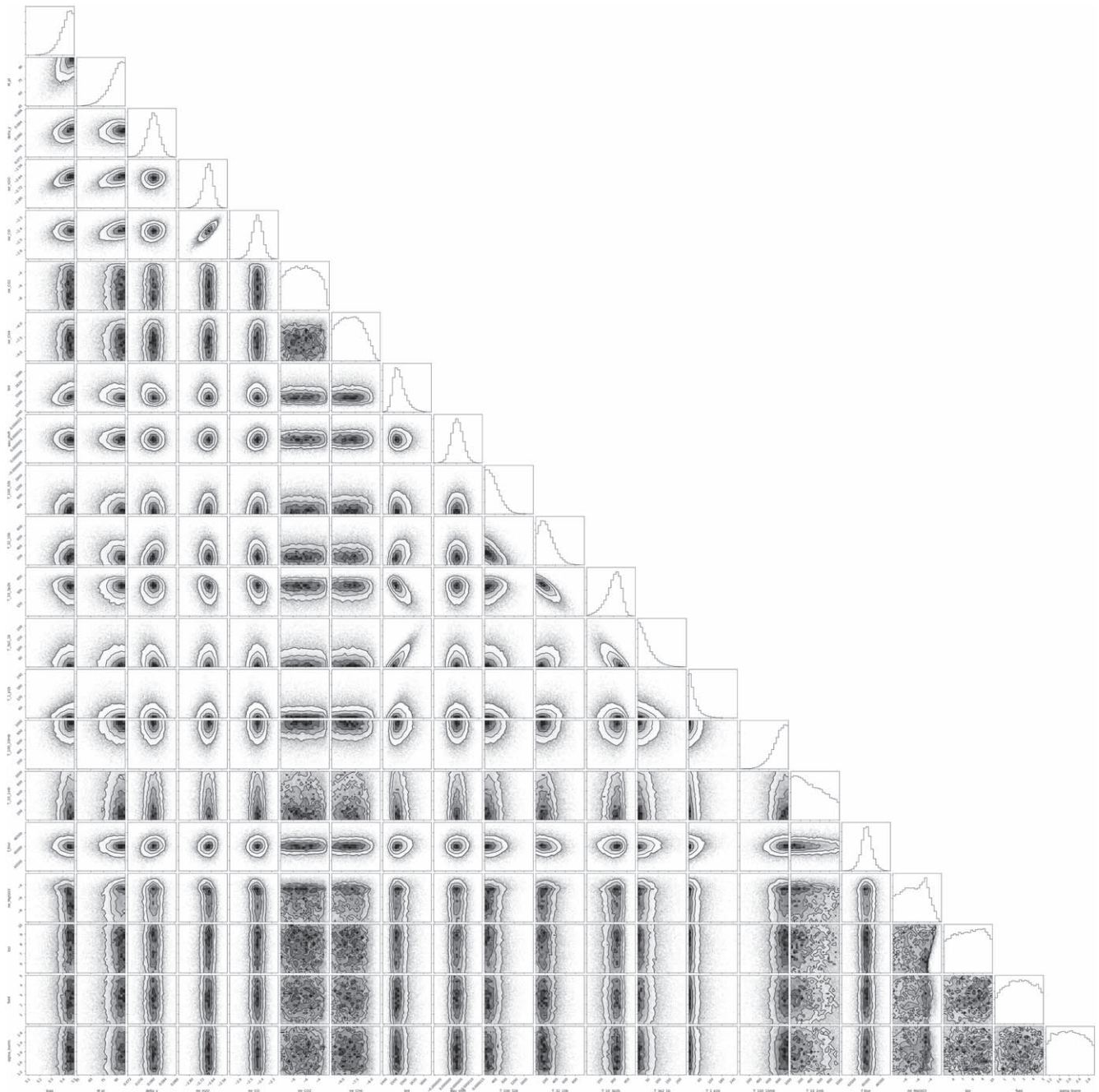


Figure 17. Posterior distributions for the retrieval for HR 7672 B with a flat prior between 10 and 100 M_{Jupiter} (see Section 6).

ORCID iDs

Ji Wang (王吉) <https://orcid.org/0000-0002-4361-8885>
 Jared R. Kolecki <https://orcid.org/0000-0002-6267-0849>
 Jean-Baptiste Ruffio <https://orcid.org/0000-0003-2233-4821>
 Jason J. Wang (王劲飞) <https://orcid.org/0000-0003-0774-6502>
 Dimitri Mawet <https://orcid.org/0000-0002-8895-4735>
 Ashley Baker <https://orcid.org/0000-0002-6525-7013>
 Geoffrey A. Blake <https://orcid.org/0000-0003-0787-1610>
 Jacques-Robert Delorme <https://orcid.org/0000-0001-8953-1008>
 Luke Finnerty <https://orcid.org/0000-0002-1392-0768>
 Michael P. Fitzgerald <https://orcid.org/0000-0002-0176-8973>
 Nemanja Jovanovic <https://orcid.org/0000-0001-5213-6207>

Anusha Pai Asnodkar <https://orcid.org/0000-0002-8823-8237>
 Arpita Roy <https://orcid.org/0000-0001-8127-5775>
 Garreth Ruane <https://orcid.org/0000-0003-4769-1665>
 Andrew Skemer <https://orcid.org/0000-0001-6098-3924>
 Nicole L. Wallack <https://orcid.org/0000-0003-0354-0187>
 Peter Wizinowich <https://orcid.org/0000-0002-1646-442X>

References

Allard, F., Homeier, D., & Freytag, B. 2012, *RSPTA*, 370, 2765
 Allard, F., Homeier, D., Freytag, B., et al. 2013, *MSAIS*, 24, 128
 Amarsi, A. M., Nissen, P. E., & Skúladóttir, Á. 2019, *A&A*, 630, A104
 Baraffe, I., Homeier, D., Allard, F., & Chabrier, G. 2015, *A&A*, 577, A42
 Baudino, J.-L., Mollière, P., Venot, O., et al. 2017, *ApJ*, 850, 150

- Boccaletti, A., Chauvin, G., Lagrange, A. M., & Marchis, F. 2003, *A&A*, **410**, 283
- Brandl, B., Bettonvil, F., van Boekel, R., et al. 2021, *Msngr*, **182**, 22
- Brandt, T. D., Dupuy, T. J., & Bowler, B. P. 2019, *AJ*, **158**, 140
- Brewer, J. M., Fischer, D. A., Valentí, J. A., & Piskunov, N. 2016, *ApJS*, **225**, 32
- Brogi, M., Line, M., Bean, J., Désert, J. M., & Schwarz, H. 2017, *ApJL*, **839**, L2
- Buchner, J., Georgakakis, A., Nandra, K., et al. 2014, *A&A*, **564**, A125
- Burningham, B., Faherty, J. K., Gonzales, E. C., et al. 2021, *MNRAS*, **506**, 1944
- Burningham, B., Marley, M. S., Line, M. R., et al. 2017, *MNRAS*, **470**, 1177
- Crepp, J. R., Johnson, J. A., Fischer, D. A., et al. 2012, *ApJ*, **751**, 97
- Crossfield, I. J. M., Biller, B., Schlieder, J. E., et al. 2014, *Natur*, **505**, 654
- da Silva, R., Milone, A. d. C., & Rocha-Pinto, H. J. 2015, *A&A*, **580**, A24
- Delorme, J.-R., Jovanovic, N., Echeverri, D., et al. 2020, *Proc. SPIE*, 11447, 114471P
- Delorme, J.-R., Jovanovic, N., Echeverri, D., et al. 2021, *JATIS*, **7**, 035006
- Dotter, A., Chaboyer, B., Jevremović, D., et al. 2007, *AJ*, **134**, 376
- Epstein, C. R., Johnson, J. A., Dong, S., et al. 2010, *ApJ*, **709**, 447
- Feroz, F., Hobson, M. P., & Bridges, M. 2009, *MNRAS*, **398**, 1601
- Finnerty, L., Buzard, C., Pelletier, S., et al. 2021, *AJ*, **161**, 104
- Fisher, C., Hoeijmakers, H. J., Kitzmann, D., et al. 2020, *AJ*, **159**, 192
- Gaia Collaboration, Brown, A. G. A., Vallenari, A., et al. 2018, *A&A*, **616**, A1
- Gaia Collaboration, Prusti, T., de Bruijne, J. H. J., et al. 2016, *A&A*, **595**, A1
- Gandhi, S., Madhusudhan, N., Hawker, G., & Piette, A. 2019, *AJ*, **158**, 228
- Gao, P., Thorngren, D. P., Lee, G. K. H., et al. 2020, *NatAs*, **4**, 951
- Gaudi, B., Roberge, A. & Habex Team/Luvoir Study Team 2021, *BAAS*, **53**, 2021n3i0301
- Gonzales, E. C., Burningham, B., Faherty, J. K., et al. 2020, *ApJ*, **905**, 46
- Horne, K. 1986, *PASP*, **98**, 609
- Husser, T. O., Wende-von Berg, S., Dreizler, S., et al. 2013, *A&A*, **553**, A6
- Jovanovic, N., Delorme, J. R., Bond, C. Z., et al. 2019, arXiv:1909.04541
- Karalidi, T., Apai, D., Marley, M. S., & Buenzli, E. 2016, *ApJ*, **825**, 90
- Kitzmann, D., Heng, K., Oreshenko, M., et al. 2020, *ApJ*, **890**, 174
- Kolecki, J. R., Wang, J., Johnson, J. A., et al. 2021, *AJ*, **162**, 125
- Konopacký, Q. M., Barman, T. S., Macintosh, B. A., & Marois, C. 2013, *Sci*, **339**, 1398
- Kramida, A., Ralchenko, Y., Reader, J. & NIST ASD Team 2020, NIST Atomic Spectra Database v5.8, <https://physics.nist.gov/asd>
- Lavie, B., Mendonça, J. M., Mordasini, C., et al. 2017, *AJ*, **154**, 91
- Line, M. R., Teske, J., Burningham, B., Fortney, J. J., & Marley, M. S. 2015, *ApJ*, **807**, 183
- Liu, M. C., Fischer, D. A., Graham, J. R., et al. 2002, *ApJ*, **571**, 519
- Luck, R. E. 2017, *AJ*, **153**, 21
- Madhusudhan, N. 2019, *ARA&A*, **57**, 617
- Maire, A. L., Molaverdikhani, K., Desidera, S., et al. 2020, *A&A*, **639**, A47
- Mann, A. W., Brewer, J. M., Gaidos, E., Lépine, S., & Hilton, E. J. 2013, *AJ*, **145**, 52
- Marley, M. S., Ackerman, A. S., Cuzzi, J. N., & Kitzmann, D. 2013, in Comparative Climatology of Terrestrial Planets, Part III: Clouds and Hazes, ed. S. J. Mackwell et al. (Tucson, AZ: Univ. of Arizona Press), 367
- Mawet, D., Bond, C. Z., Delorme, J. R., et al. 2018, *Proc. SPIE*, 10703, 1070306
- Mawet, D., Fitzgerald, M., Konopacký, Q., et al. 2019, *BAAS*, **51**, 134
- Mollière, P., Stolker, T., Lacour, S., et al. 2020, *A&A*, **640**, A131
- Mollière, P., van Boekel, R., Bouwman, J., et al. 2017, *A&A*, **600**, A10
- Mollière, P., Wardenier, J. P., van Boekel, R., et al. 2019, *A&A*, **627**, A67
- Nelson, T., Ting, Y.-S., Hawkins, K., et al. 2021, *ApJ*, **921**, 118
- Palme, H., Lodders, K., & Jones, A. 2014, in Solar System Abundances of the Elements, ed. A. M. Davis, Vol. 2 (Amsterdam: Elsevier), 15, <https://par.nsf.gov/servlets/purl/10036398>
- Parmentier, V., & Guillot, T. 2014, *A&A*, **562**, A133
- Parmentier, V., Guillot, T., Fortney, J. J., & Marley, M. S. 2015, *A&A*, **574**, A35
- Peretti, S., Ségransan, D., Lavie, B., et al. 2019, *A&A*, **631**, A107
- Piette, A. A. A., & Madhusudhan, N. 2020, *MNRAS*, **497**, 5136
- Rasmussen, K. C., Brogi, M., Rahman, F., et al. 2021, arXiv:2108.12057
- Rickman, E. L., Ségransan, D., Hagelberg, J., et al. 2020, *A&A*, **635**, A203
- Saumon, D., & Marley, M. S. 2008, *ApJ*, **689**, 1327
- Snedden, C. 1973, *ApJ*, **184**, 839
- Tremblin, P., Chabrier, G., Baraffe, I., et al. 2017, *ApJ*, **850**, 46
- Villanueva, G. L., Smith, M. D., Protopapa, S., Faggi, S., & Mandell, A. M. 2018, *QSR*, **217**, 86
- Waldmann, I. P., Tinetti, G., Rocchetto, M., et al. 2015, *ApJ*, **802**, 107
- Wang, J., Wang, J. J., Ma, B., et al. 2020, *AJ*, **160**, 150
- Zhang, Z., Liu, M. C., Marley, M. S., Line, M. R., & Best, W. M. J. 2021, *ApJ*, **916**, 53